Coupled continuous–discrete formulation based on microplane and strong discontinuity models for representing non-orthogonal intersecting cracks

Santosh Kakarla, Giuseppe Rastiello, Benjamin Richard, Cédric Giry

To cite this version:

Santosh Kakarla, Giuseppe Rastiello, Benjamin Richard, Cédric Giry. Coupled continuous–discrete formulation based on microplane and strong discontinuity models for representing non-orthogonal intersecting cracks. Engineering Fracture Mechanics, 2021, 245, pp.107565. 10.1016/j.engfracmech.2021.107565 . hal-03164511

HAL Id: hal-03164511
https://hal.science/hal-03164511

Submitted on 9 Mar 2023

Continuous-discrete coupling formulation based on microplane and strong discontinuity models for representing non-orthogonal intersecting cracks

Santosh Kakarla[a], Giuseppe Rastiello[a], Benjamin Richard[c,*], Cédric Giry[b]

[a] *Université Paris-Saclay, CEA, Service d'études mécaniques et thermiques*
91191 Gif-sur-Yvette Cedex, France

[b] *Université Paris-Saclay, ENS Paris-Saclay, CNRS, LMT - Laboratoire de Mécanique et Technologie*
91190, Gif-sur-Yvette, France.

[c] *Institut de Radioprotection et de Sûreté Nucléaire (IRSN), PSN-EXP/SES/LMAPS*
92262 Fontenay-aux-Roses Cedex, France

Abstract

Fracture process in quasi-brittle materials is governed by the strain localization phenomenon which involves the formation of localized damage zones and cohesive cracks. In this work, we present numerical tools to model strain localization from the onset of localized damage to the formation and propagation of multiple intersecting cracks. Two main ingredients are used for this purpose: (i) a microplane model, to describe the initial anisotropic damage phase; (ii) the strong discontinuity method, to introduce cracks as strong discontinuities in the damaged continuum using the Embedded Finite Element Method (E-FEM). Here, we formulate the microplane microdamage model in a thermodynamic framework using simple constitutive laws on each microplane. In order to describe multiple intersecting cracks, we extend the standard E-FEM to accommodate two strong discontinuities. The coupling between microplane microdamage model with the strong discontinuity model is achieved using a transition method based on the energy equivalence between both models. Exploiting the anisotropic description provided by the microplane model, transition criteria are formulated based on the quantities defined on each microplane. The proposed methodologies are illustrated using several elementary test cases that involve both simple and complex stress-strain states.

Keywords: multiple cracks, microplane model, embedded finite element method, damage-to-fracture transition

Nomenclature

Acronyms

BVP	Boundary Value Problem
CST	Constant Strain Triangle
DOF	Degree of Freedom
E-FEM	Embedded Finite Element Method
KOS	Kinematically Optimal Symmetric
SKON	Statically and Kinematically Optimal Nonsymmetric
SOS	Statically Optimal Symmetric
X-FEM	eXtended Finite Element Method

Domain notations

$(\mathcal{B}_e^h)^+$, $(\mathcal{B}_e^h)^-$	Sub-domains of a finite element crossed by a discontinuity
$\mathcal{B}$	Domain of the material
$\mathcal{B}^+$, $\mathcal{B}^-$	Sub-domains of the body crossed by a discontinuity

---

[*] Corresponding author
Email addresses: `santosh.kakarla@ens-paris-saclay.fr` (Santosh Kakarla), `giuseppe.rastiello@cea.fr` (Giuseppe Rastiello), `benjamin.richard@irsn.fr` (Benjamin Richard), `cedric.giry@ens-paris-saclay.fr` (Cédric Giry)

Preprint submitted to Engineering Fracture Mechanics *November 23, 2020*

$\mathcal{B}_e^h$	Finite element of the discretized body
$\Gamma_{d_{i=1,2}}$	Discontinuity surfaces of the first and the second crack
$\mathcal{E}_{i=1,2}$	Set of finite elements crossed by the first and the second discontinuity
Ω	Domain of microplane system
Ω^α	A microplane in the disk microplane system
$\partial_t\mathcal{B}$	Boundary on which the traction is applied
$\partial_u\mathcal{B}$	Boundary on which the displacement is applied
n_{elem}	Number of finite elements in a discretized body

Vectors and matrices

$\mathbf{B}$	Gradient matrix
$\mathbf{d}$	Discretized displacement vector
$\mathbf{d}^*$	Discretized virtual displacement vector
$\mathbf{e}$	Discretized enhanced displacement vector
$\mathbf{e}^*_{i=1,2}$	Discretized virtual enhanced displacement vectors associated with first and second crack
$\mathbf{G}^*_{i=1,2}$	Virtual enhanced shape functions matrices associated with first and second crack
$\mathbf{G}_{i=1,2}$	Enhanced shape functions matrices associated with first and second crack
$\mathbf{H}_{\Gamma_d}$	Matrix formed using the Heaviside function
$\mathbf{N}_a$	Elementary shape functions matrix
$\mathbf{N}_{c_{i=1,2}}$	Shape functions matrix for the enhanced displacement fields associated with the first and second crack
$\mathbf{P}_{i=1,2}$	Projection matrices at the first and the second discontinuity
$\mathbf{F}_{ext}$	Column vector of external forces
$\mathbf{F}_{int}$	Column vector of internal forces
$\mathbf{f}_{int}$	Column vector of internal forces associated with the traction continuity condition
$\tilde{\mathbf{K}}$	Global stiffness matrix after static condensation
$\tilde{\mathbf{F}}_{int}$	Internal force vector after static condensation

Space notations

$\mathcal{L}^2$	Set of square-integrable functions
E	Admissible space of the enhanced strain field
$\mathsf{E}^{\perp\mathsf{S}}$	Admissible space of enhanced strain field orthogonal to the stress field
S	Admissible space of the stress field
U	Admissible set of the displacement field
U_0	Admissible space of the applied displacement field
Ω^1	Set of microplanes in loading
Ω^2	Set of microplanes in unloading
H^1	First-order Sobolev spaces
H^1_0	Homogeneous first-order Sobolev spaces
$R(\mathbf{x}_{i=1,2})$	Orthonormal basis

Functions and operators

A	Assembly operator
$\cdot$	Contraction operator
$:$	Double contraction operator
δ_{Γ_d}	Dirac delta function
∇^s	Symmetric part of the gradient
H_{Γ_d}	Heaviside function
$\langle(\bullet)\rangle^+$	Positive part of $(\bullet)$
$\mathbf{L}^\alpha$	Tangential projection operator of a microplane
$\mathbf{M}^\alpha$	Normal projection operator of a microplane
$\mathcal{F}$	Constitutive relationship between stress and strain
div	Divergence operator
meas$(\bullet)$	Measure of $(\bullet)$
max$(\bullet)$	Maximum value of $(\bullet)$
$H_{[\![u]\!]_{n_{i=1,2}}}$	Heaviside functions associated with the first and second crack
$h_{i=1,2}$	Discrete constitutive laws for the first and second crack
q	Softening function of the microplane microdamage model

Scalar variables

$(\sigma_I)_{\mathrm{tr}}$	Maximum principal stress at transition
α	Angle of the normal to a microplane in the disk microplane system
β	Parameter of the microplane microdamage model
β_{cr}	Model parameter of the traction–separation law
$[\![u]\!]_n$	Normal component of the displacement jump at a crack surface
$[\![u]\!]_s$	Tangential component of the displacement jump at a crack surface
ω^α	Microdamage variable
$\tilde{\epsilon}^\alpha$	Equivalent strain on a microplane
$\epsilon_l^{\alpha*}$	Virtual tangential component of strain on a microplane in the disk microplane system
$\epsilon_m^{\alpha*}$	Virtual normal component of

	strain on a microplane in the disk microplane system
ϵ_l^α	Tangential component of strain on a microplane in the disk microplane system
ϵ_m^α	Normal component of strain on a microplane in the disk microplane system
γ_ϵ^{asy}	Asymptotic value of the rotation of the maximum principal strain axis with respect to the vertical direction
γ_σ^{asy}	Asymptotic value of the rotation of the maximum principal stress axis with respect to the vertical direction
γ_ϵ	Rotation of the maximum principal strain axis with respect to the vertical direction
γ_σ	Rotation of the maximum principal stress axis with respect to the vertical direction
$\hat{\phi}_S$	Available energy for the crack
$\hat{\phi}_V$	Dissipated volumetric energy
$\hat{\phi}_V^\alpha$	Dissipated volumetric energy on a microplane
$\hat{\phi}_{S_{i=1,2}}$	Available energy for first and second crack
κ^α	History variable on a microplane
κ_{cr}	History variable associated to the traction–separation law
λ	Lame's constant
$\left(\epsilon_l^{\alpha+}\right)$	Positive tangential strain component on a microplane
$\left(\epsilon_m^{\alpha+}\right)$	Positive normal strain component on a microplane
$(\phi_V^\alpha)_{tr}$	Volumetric energy dissipation on a microplane at transition pseudo-time
$[\![u]\!]_{n_{i=1,2}}$	Normal components of the displacement jump at the first and the second crack surface
$[\![u]\!]_{s_{i=1,2}}$	Tangential components of the displacement jump at the first and the second crack surface
μ	Lame's constant
ν	Poisson's ratio
ω^α	Microdamage variable on a microplane
ω_{tr}^α	Microdamage variable on a microplane at transition pseudo-time
ϕ_S	Energy dissipation at the crack
ϕ_V	Energy dissipation of a unit volume
ϕ_V^α	Volumetric energy dissipation on a microplane
ψ	Free energy of a unit volume
ψ_0^α	Elastic part of free energy on a microplane
ψ_S	Helmholtz free energy at a crack surface
ρ	Density of the material
σ_l^α	Tangential component of strain on a microplane in the disk microplane system
σ_m^α	Normal component of stress on a microplane in the disk microplane system
$\tilde{\epsilon}_0^\pi$	Threshold equivalent strain on a microplane
B	Regularized parameter of microplane microdamage model
d_{cr}	Damage-like internal variable of the traction–separation law
E	Young's modulus
E_l	Elastic stiffness component in tangential direction of a microplane
E_m	Elastic stiffness component in normal direction of a microplane
f_t	Uniaxial tensile strength of the material
f_{cr}	Yield surface of the traction–separation law
$F_{i=1,2}$	Component of force in orthonormal basis
$flag$	Boolean variable to store information of crack activation
$flag_{i=1,2}$	Boolean variables to store information of activation of first and second crack
G_f	Fracture energy of the material
g_f	Energy dissipation density of a unit volume
g_f^π	Energy dissipation density of a microplane
l_c	Characterisitc length
N	Number of pseudo-time steps
N^α	Number of microplanes of a numerical integration scheme
t	Pseudo-time instant
t_n	Normal component of traction at the crack surface
t_{tr}	Pseudo-time step at transition
$u_{i=1,2}$	Component of displacement in orthonormal basis
W^α	Weight corresponding to numerical integration on a microplane
Y^α	Conjugate variable associated with the internal variable on a microplane

Tensor variables	
$\mathbb{E}$	Hooke's elastic stiffness tensor
$\boldsymbol{\epsilon}$	Strain tensor
$\boldsymbol{\epsilon}^*$	Virtual strain field
$\boldsymbol{I}$	Second-order identity tensor
$\mathbf{K}$	Stiffness tensor of the traction–separation law
$\nabla^s \bar{\mathbf{u}}$	Continuous part of the strain field
$\boldsymbol{\sigma}$	Stress tensor fulfilling the constitutive law equations
$\tilde{\boldsymbol{\sigma}}$	Statically admissible stress tensor
$\tilde{\boldsymbol{\sigma}}^*$	Virtual stress field
Vector variables	
$\bar{\mathbf{u}}$	Continuous part of the displacement field
$\mathbf{u}$	Displacement field
$\mathbf{u}^*$	Virtual displacement field
$\mathbf{u}_0$	Applied displacement
$[\![\mathbf{u}]\!]$	Displacement jump field
$\mathbf{l}^\alpha$	Tangent to a microplane in the disk microplane system
$\mathbf{m}^\alpha$	Normal to a microplane in the disk microplane system
$\mathbf{n}_{i=1,2}$	Normal to the first and the second crack
$\mathbf{x}$	Position of a point in the domain of the material
$\mathbf{p}$	Normal of the boundary
$\mathbf{t}$	Traction at the discontinuity
$\mathbf{t}_0$	Applied traction

1. Introduction

The fracture process in quasi-brittle materials is a complex physical phenomenon [1]. It starts with the initiation of distributed microcracking. Then, strain localization is observed with the development of microcracking in the fracture process zone. Energy dissipation takes place in this zone while the material in the surrounding releases elastic energy previously stored. Finally, the microcracks coalesce to form macrocracks. Several efficient numerical methods are dedicated to crack initiation and propagation modeling in solids. However, simulation of the formation of multiple crack patterns, crack interactions, and crack closure effects during cyclic loading is still a challenging issue. This paper exposes an innovative approach to model the complex phenomenon of formation of multiple cracks in quasi-brittle materials subjected to complex loading.

To achieve this objective, it is essential to consider anisotropic non-linear behavior. In the literature, several techniques have been proposed for modeling anisotropic microcracking processes. For instance, we can cite numerical approaches based on elasto-plasticity such as [2, 3], smeared crack models (fixed crack [4], rotating crack [5] and multiple fixed cracks [6] formulations), isotropic [7, 8] and anisotropic [9, 10] continuum damage models, microplane models [11, 12, 13, 14]. Among these works, microplane models can describe the anisotropic nature of cracking in concrete by describing the material degradation in several directions.

In microplane models [15, 16], the unit volume is represented by a spherical microplane system. The framework consists in the projection of strains, termed as *kinematic constraint*, on the elementary planes belonging to the microplane system to obtain its components in the normal and the tangential directions. The corresponding stress components are obtained by postulating constitutive laws on each microplane. Then the principle of virtual work is used to obtain the continuum stress tensor from its microplane counterparts as a spherical integral [12]. For the analysis of planar members, [17] proposes a simplification of this original framework by considering a disk microplane system to represent the unit volume. For two-dimensional (2D) problems, this formulation provides simple modeling and is less time consuming from a computational viewpoint than the spherical microplane system. Nevertheless, the extraction of fine information about cracking from continuum strain-softening models involves appropriate post-processing techniques [18, 19].

To avoid the use of additional tools to extract information related to the cracking process (location, crack opening, and crack spacing) and to describe more precisely the displacement discontinuity occurring at failure, numerical methods have been developed to describe cracking explicitely by assuming a discontinuous kinematics. The discontinuous kinematics models aim to capture the failure in quasi-brittle materials by incorporating the strain (weak) and/or displacement (strong) discontinuities inside the continuum [20, 21].

In the context of the Finite Elements Method (FEM), these discontinuities are modeled by introducing additional Degrees Of Freedom (DOFs) pertaining to the localization modes. These additional DOFs are interpolated using enhanced shape functions. The most popular numerical methods are the Embedded

FEM (E-FEM) [22, 20] and the eXtended FEM (X-FEM) [23, 24]. For the E-FEM, the additional DOFs are embedded [25, 26] inside the localized finite elements, and the global DOFs of the discretized finite element model remain unchanged. For the X-FEM [23, 27], the additional DOFs are supported by the nodes of the localized finite elements, leading to an increase in the global DOFs number. Thus, E-FEM can be implemented in existing finite element codes in a less intrusive manner than X-FEM. While the discontinuous kinematics models provide an explicit description of cracking, the techniques mentioned above failed to describe multiple cracks. For this purpose, specific mesh-based approaches can be found out from the literature such as lattice models [28, 29, 30, 31]. Although these techniques can be used to estimate fine cracking properties, they are also known to be mesh-sensitive (for coarse meshes), and implementing specific dissipative local mechanisms is not straightforward. For these reasons, the choice not to focus on these techniques has been made in this study.

In the literature, several models that performs a damage-to-fracture transition either in linear elastic fracture mechanics [32] or in cohesive crack framework [33, 34] are proposed. These models describe the entire strain localization process from localized damage to the initiation and propagation of cracks. In general, the coupling between implicit and explicit cracking descriptions can be established either in a thermodynamics framework [35] or using the strong discontinuity kinematics [36, 26]. In the first approach, the damage-to-fracture transition is achieved by assuming that the total mechanical energy of the body is the same for any modeling strategy [35]. This is known as energy equivalence approach. In the second approach, the so-called strong discontinuity analysis [37, 38] is performed to introduce a crack in the media. In the present work, we follow this first approach.

In this article, we first present the general framework of the microplane models and expose a specific microplane microdamage model within a thermodynamic framework. Second, we present the strong discontinuity framework which is numerically implemented using E-FEM. An extension of the standard E-FEM also proposed to account for multiple intersecting cracks within the same finite element. Finally, the microplane model and E-FEM are coupled within a transition framework using the energy equivalence approach.

2. Microplane microdamage model

According to microplane models, anisotropic damage is described by sampling the material behavior in several possible directions. In the simplified microplane representation that is considered in this work, microplanes are located on the circumference of the unit disk[1] Ω (Fig. 1). Here, the disk microplane system under the plane strain assumptions is used to represent the unit volume. Hence, the stress and strain components in the direction of $\mathbf{x}_3$ (Fig. 1) are assumed to be independent of the microplane system. The model is derived in the plane ($\mathbf{x}_1$, $\mathbf{x}_2$). In particular, we define a scalar isotropic damage constitutive law on each microplane and derive the constitutive model of the unit volume. Different steps involved in the formulation are presented here.

2.1. Projection of strain tensor

Let us consider a microplane Ω^α whose normal vector (denoted by $\mathbf{m}^\alpha$) makes an angle α with reference axis $\mathbf{x}_1$ (Fig. 1). The tangent vector to Ω^α is denoted by $\mathbf{l}^\alpha$ ($\mathbf{l}^\alpha \cdot \mathbf{m}^\alpha = 0$). According to the kinematic constraint, the normal (ϵ_m^α) and the tangential (ϵ_l^α) strain components at Ω^α are obtained as the projection of the strain tensor ($\boldsymbol{\epsilon}$):

$$\epsilon_m^\alpha = \mathbf{m}^\alpha \cdot \boldsymbol{\epsilon} \cdot \mathbf{m}^\alpha = \mathbf{M}^\alpha : \boldsymbol{\epsilon} \quad \text{and} \quad \epsilon_l^\alpha = \mathbf{l}^\alpha \cdot \boldsymbol{\epsilon} \cdot \mathbf{m}^\alpha = \mathbf{L}^\alpha : \boldsymbol{\epsilon} \tag{1}$$

where, symbol "$\cdot$" denotes the simple contraction between tensors and the second-order tensors $\mathbf{M}^\alpha = \mathbf{m}^\alpha \otimes \mathbf{m}^\alpha$ and $\mathbf{L}^\alpha = \left(\mathbf{l}^\alpha \otimes \mathbf{m}^\alpha + \mathbf{m}^\alpha \otimes \mathbf{l}^\alpha\right)/2$ are the projection operators. In these definitions, symbol "$\otimes$" denotes the dyadic product between vectors.

---

[1] The planar surfaces with outward normal parallel to $\mathbf{x}_3$ (Fig. 1) are not included in the system.

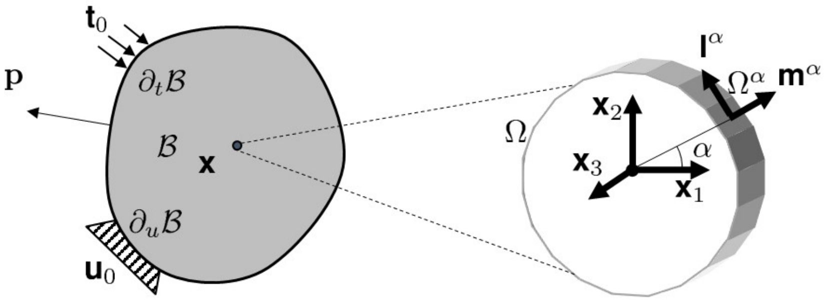

Figure 1: Representation of unit volume using the disk microplane system

2.2. Thermodynamic framework

In this work, damage is considered as the only dissipative mechanism on a given microplane. Furthermore, we adopt a microplane microdamage model employing a single microdamage variable [39, 40]. From a numerical viewpoint, such a choice leads to a more computationally efficient formulation as it is discussed later on.

Free energy. Following [41], an integral relationship between the free energy potential at the unit volume (ψ) on each microplane (ψ^α) using the microdamage scalar variable ($\omega^\alpha \in [0, 1[$) is written as:

$$\rho\psi = \frac{1}{\pi}\int\limits_{\Omega} \rho\psi^\alpha \; dS, \qquad \rho\psi^\alpha = (1-\omega^\alpha)\,\rho\psi_0^\alpha \qquad \rho\psi_0^\alpha = \frac{1}{2}\left[E_m\left(\epsilon_m^\alpha\right)^2 + E_l\left(\epsilon_l^\alpha\right)^2\right] \tag{2}$$

where $\rho\psi_0^\alpha$ is the stored elastic energy on each microplane. Here, E_m and E_l are the elastic constants for each microplane in normal and tangential directions, respectively. The expressions of E_m and E_l are obtained in terms of macroscopic Young's modulus (E) and Poisson's ratio (ν) (see Appendix B).

State variables. The normal (σ_m^α) and tangential (σ_l^α) stresses on Ω^α are obtained as the first partial derivatives of ψ^α with respect to the normal and tangential strain, respectively:

$$\sigma_m^\alpha = \rho\frac{\partial\psi^\alpha}{\partial\epsilon_m^\alpha} = (1-\omega^\alpha)\,E_m\epsilon_m^\alpha \quad \text{and} \quad \sigma_l^\alpha = \rho\frac{\partial\psi^\alpha}{\partial\epsilon_l^\alpha} = (1-\omega^\alpha)\,E_l\epsilon_l^\alpha \tag{3}$$

Furthermore, the microplane energy release rate (Y^α) is obtained as a conjugate of ω^α as:

$$Y^\alpha = -\rho\frac{\partial\psi^\alpha}{\partial\omega^\alpha} = \frac{1}{2}\left[E_m\left(\epsilon_m^\alpha\right)^2 + E_l\left(\epsilon_l^\alpha\right)^2\right] \tag{4}$$

In microplane models, $\boldsymbol{\sigma}$ can be obtained either by imposing equivalence of the virtual works computed using macroscopic quantities and their microplane counterparts [11] or, within a thermodynamic framework, using constitutive laws written at the microplane level [41, 14]. However, in the absence of deviatoric/volumetric split, both approaches lead to the same expression of the stress tensor [41]. Hence, by following the thermodynamic approach and using Eqs. (2) and (3), we obtain:

$$\boldsymbol{\sigma} = \rho\frac{\partial\psi}{\partial\boldsymbol{\epsilon}} = \frac{1}{\pi}\int\limits_{\Omega}\frac{\partial\left(\rho\psi^\alpha\right)}{\partial\boldsymbol{\epsilon}}\; dS = \frac{1}{\pi}\int\limits_{\Omega}\rho\left(\frac{\partial\psi^\alpha}{\partial\epsilon_m^\alpha}\frac{\partial\epsilon_m^\alpha}{\partial\boldsymbol{\epsilon}} + \frac{\partial\psi^\alpha}{\partial\epsilon_l^\alpha}\frac{\partial\epsilon_l^\alpha}{\partial\boldsymbol{\epsilon}}\right)\; dS = \frac{1}{\pi}\int_{\Omega}\left(\sigma_m^\alpha\mathbf{M}^\alpha + \sigma_l^\alpha\mathbf{L}^\alpha\right)\; dS \tag{5}$$

Rate of energy dissipation. The Clausius-Duhem-Trusdell inequality for a unit volume is written as, $\dot{\phi}_V = \boldsymbol{\sigma} : \dot{\boldsymbol{\epsilon}} - \rho\dot{\psi} \geq 0$, where, $\dot{\phi}_V$ is the rate of energy dissipation for a unit volume:

$$\dot{\phi}_V = \frac{1}{\pi}\int\limits_{\Omega} \dot{\phi}_V^{\alpha}\ dS \qquad \dot{\phi}_V^{\alpha} = -Y^{\alpha}\dot{\omega}^{\alpha} \geq 0 \tag{6}$$

where, $\dot{\phi}_V^{\alpha}$ is the rate of energy dissipation on each microplane.

Flow rules. The evolution of ω^{α} is defined as:

$$\omega^{\alpha} = 1 - \frac{q(\kappa^{\alpha})}{\kappa^{\alpha}} \quad \text{with} \quad q(\kappa^{\alpha}) = \tilde{\epsilon}_0^{\pi} \exp^{(-B(\kappa^{\alpha} - \tilde{\epsilon}_0^{\pi}))} \tag{7}$$

where, B is a material parameter controlling the softening branch and κ^{α} is an internal (history) variable. Here, κ^{α} is defined as the historical maxima of an equivalent strain measure ($\tilde{\epsilon}^{\alpha}$) on each microplane as:

$$\kappa^{\alpha} = \max_t(\tilde{\epsilon}_0^{\pi}, \tilde{\epsilon}^{\alpha}(t)) \tag{8}$$

where $\tilde{\epsilon}_0^{\pi}$ is a threshold expressed in terms of equivalent strain which has to be overcome to activate microdamage, and t is the current pseudo-time. Note that in the following, superscript π will always be used to denote microplane quantities independent of the chosen Ω^{α}.

In the formulation proposed in this work, $\tilde{\epsilon}^{\alpha}$ is defined as:

$$\tilde{\epsilon}^{\alpha} = \sqrt{\left(\epsilon_m^{\alpha+}\right)^2 + \beta\left(\epsilon_l^{\alpha+}\right)^2} = \sqrt{\left(\mathbf{M}^{\alpha} : \langle\boldsymbol{\epsilon}\rangle^{+}\right)^2 + \beta\left(\mathbf{L}^{\alpha} : \langle\boldsymbol{\epsilon}\rangle^{+}\right)^2} \tag{9}$$

where $\langle\boldsymbol{\epsilon}\rangle^{+}$ is defined as the positive part of the continuum strain tensor. Here, $\beta \geq 0$ is a parameter accounting for the contribution of the tangential strain to the growth of microdamage.[2] Since cracking in quasi-brittle materials is mainly controlled by extensions [7] (either direct or indirect), such a choice seems consistent from a physical viewpoint.

Yield function. The yield function (denoted by f^{α}) is expressed in terms of $\tilde{\epsilon}^{\alpha}$. The Kuhn-Tucker loading-unloading conditions are written for each microplane as:

$$f^{\alpha} = f^{\alpha}(\tilde{\epsilon}^{\alpha}) = \tilde{\epsilon}^{\alpha} - \kappa^{\alpha} \quad \text{and} \quad \dot{\omega}^{\alpha} \geq 0,\ f^{\alpha} \leq 0,\ \dot{\omega}^{\alpha} f^{\alpha} = 0 \tag{10}$$

Density of energy dissipation. In literature [43], the fracture energy per unit volume is calculated by considering a uniaxial loading path under a one-dimensional (1D) assumption. However, to obtain the density of energy dissipation of a unit volume under 2D plane strain assumption, we consider that g_f is dissipated by the unit volume at the end of a multi-directional loading process. Owing to the representation of the unit volume using microplane system, the energy which is dissipated at the end of the fracture process (g_f) is expressed by using the expended power on each microplane (g_f^{α}) as:

$$g_f = \int\limits_0^{\infty} \boldsymbol{\sigma} : \dot{\boldsymbol{\epsilon}}\ dt = \frac{1}{\pi}\int\limits_{\Omega} g_f^{\alpha}\ dS \quad \text{with} \quad g_f^{\alpha} \equiv \int\limits_0^{\infty} \left(\sigma_m^{\alpha}\dot{\epsilon}_m^{\alpha} + \sigma_l^{\alpha}\dot{\epsilon}_l^{\alpha}\right)\ dt \tag{11}$$

where $\dot{\epsilon}_m^{\alpha} = \mathbf{M}^{\alpha} : \dot{\boldsymbol{\epsilon}}$ and $\dot{\epsilon}_l^{\alpha} = \mathbf{L}^{\alpha} : \dot{\boldsymbol{\epsilon}}$. Here, we use the property that microplanes do not interact with each other as we interchange the integration over the time domain and over the microplane system.

---

[2] In the proposed microplane microdamage model, the coupling between different components of strain is necessary because we use a single microdamage variable to drive the dissipation in both the normal and tangential directions. This would not have been necessary if one had used more than one microdamage variable [13, 42].

Due to the assumption of equal parameters of elasticity and damage evolution, for each microplane, g_f^α is the same on all the microplanes (i.e., $g_f^\alpha = g_f^\pi$). Finally, by performing the analytical integration of Eq. (11), we end up with the following relationship between the density of energy dissipation on each microplane and the one related to the unit volume:

$$g_f^\pi = \frac{g_f}{2} \tag{12}$$

2.3. Energetic regularization

The use of softening constitutive law in the context of the FEM does not provide objective results when describing a localization phenomenon like cracking. Consequently, a characteristic length (l_c) is required to obtain mesh independent solutions. In the literature, microplane models are regularized using crack band [44], nonlocal [45] or gradient enhanced [46] approaches, among others. These formulation restore mesh independence of the results with respect to the spatial discretization. Depending on the technique, they impose additional computational costs due to the need for computing averaged quantities that drive the damage evolution (e.g., in nonlocal models) or to solve an additional equation (e.g., in gradient formulations).

An alternative approach commonly used in structural mechanics [47, 48] in order to reduce mesh sensitivity, with a moderate computational cost, is based upon the so-called energetic regularization technique [49, 43]. According to this approach, a length l_c (proportional to the mesh size and depending on the type of finite element [50, 47]) is introduced into the constitutive equations using a direct relationship between the volumetric (g_f) and the surface (G_f – considered as a material parameter) energy densities as, $g_f = G_f/l_c$. Now, using Eq. (12) we obtain the relation between volumetric energy density on each microplane and the surface energy density as, $g_f^\pi = G_f/2l_c$.

Using this relation, we derive a regularized damage evolution model (Appendix Appendix A). In the later sections, we also exploit this relation to calculate the residual energy at each stage of the loading cycle on each microplane.

2.4. Integration of microplane quantities

In this work, given the symmetry of the domain, and because σ_m^α and σ_l^α are periodic with period π, the integration in Eq. (5) is restricted to the contour of a unit semi-circle. The half microplane system is then discretized as the set of N^α microplanes of normal $\mathbf{m}^\alpha$, such that one microplane is always orthogonal to $\mathbf{x}_1$ (i.e., $\alpha = 0°$). As a consequence, the inclination of the *i-th* microplane with respect to the horizontal axis is $(i-1)180°/N^\alpha$. Alternatively, if both microplanes whose normal corresponds to $\alpha = 0°$ and $\alpha = 180°$, the inclination of the i-th microplane with respect to the horizontal axis can be obtained as $(i-1)180°/(N^\alpha - 1)$.

The stress tensor $\boldsymbol{\sigma}$ is finally obtained by using a numerical integration composite midpoint rule:

$$\boldsymbol{\sigma} = \frac{2}{\pi}\sum_{1}^{N^\alpha} \left(\sigma_m^\alpha \mathbf{M}^\alpha + \sigma_l^\alpha \mathbf{L}^\alpha\right) W^\alpha \tag{13}$$

where, $W^\alpha = \pi/N^\alpha$ is the weight associated to each microplane.

3. Strong discontinuity framework and embedded finite element method (E-FEM)

Here, we describe the modeling of media crossed by cracks using the strong discontinuity approach in the E-FEM framework. The problem of a quasi-brittle medium developing multiple intersecting discontinuities in quasi-static case is treated within the E-FEM in [51]. In this paper, the discontinuous part of the displacement is obtained as the sum of displacement jumps at the multiple discontinuities. Besides, the local equilibrium is fulfilled by satisfying the traction continuity conditions on each discontinuity surface. We present here the kinematics and the Boundary Value Problem (BVP) in case of two intersecting strong discontinuities which is then solved by extending the standard E-FEM.

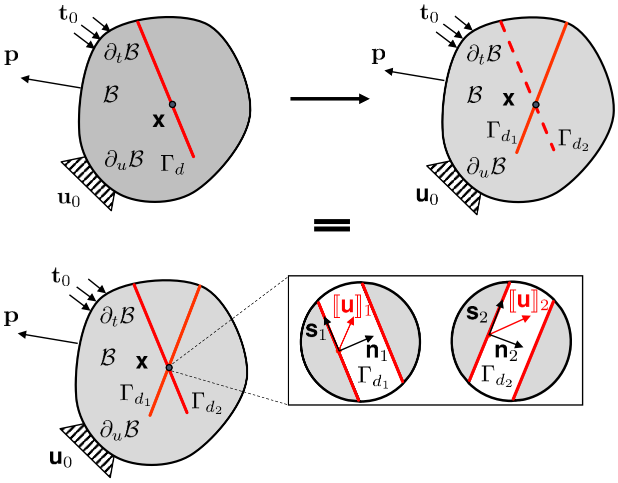

Figure 2: Extension of strong discontinuity kinematics - a body ($\mathcal{B}$) with multiple intersecting discontinuities Γ_{d_1} and Γ_{d_2}

3.1. Kinematics and boundary value problem

Let us consider a body $\mathcal{B}$ crossed by a single discontinuity Γ_{d_1} whose normal is denoted by $\mathbf{n}_1$. Now, let us assume that during the loading history, a second crack Γ_{d_2} with normal $\mathbf{n}_2$ is localized (Fig. 2). Here, Γ_{d_1} and Γ_{d_2} divide the domain into two pairs of sub-domains each, denoted by, $\mathcal{B}_1^+$, $\mathcal{B}_1^-$ and $\mathcal{B}_2^+$, $\mathcal{B}_2^-$. Let $\partial\mathcal{B}$ be the boundary of $\mathcal{B}$ and let us denote $\mathbf{p}$ its outer normal vector. Here, the main underlying assumption is that the state of the body with two discontinuities is obtained as the superposition of the states with each discontinuity. Interaction between discontinuities is then modeled through coupled traction continuity conditions.

The kinematic response at any material point $\mathbf{x} \in \mathcal{B}$ is characterized by an infinitesimal displacement field, $\mathbf{u}$ which consists of a continuous part $\bar{\mathbf{u}}$ and discontinuous parts $[\![\mathbf{u}]\!]_1$ and $[\![\mathbf{u}]\!]_2$ associated with Γ_{d_1} and Γ_{d_2} respectively as:

$$\mathbf{u} = \bar{\mathbf{u}} + \mathcal{H}_{\Gamma_{d_1}}[\![\mathbf{u}]\!]_1 + \mathcal{H}_{\Gamma_{d_2}}[\![\mathbf{u}]\!]_2 \tag{14}$$

where, $\mathcal{H}_{\Gamma_{d_1}}(\mathbf{x})$ and $\mathcal{H}_{\Gamma_{d_2}}(\mathbf{x})$ are the Heaviside functions at Γ_{d_1} and Γ_{d_2} respectively. $\mathcal{H}_{\Gamma_{d_1}}(\mathbf{x})$ and $\mathcal{H}_{\Gamma_{d_2}}(\mathbf{x})$ are equal to 1 on $\mathcal{B}_1^+$, $\mathcal{B}_2^+$ and 0 on $\mathcal{B}_1^-$, $\mathcal{B}_2^-$, respectively.

Under the small perturbations assumption, the infinitesimal strain tensor $\boldsymbol{\epsilon}$ compatible with the displacement field is then defined as:

$$\boldsymbol{\epsilon} = \underbrace{\nabla^s\bar{\mathbf{u}} + \mathcal{H}_{\Gamma_{d_1}}\nabla^s[\![\mathbf{u}]\!]_1 + \mathcal{H}_{\Gamma_{d_2}}\nabla^s[\![\mathbf{u}]\!]_2}_{\text{regular part}} + \underbrace{\left(\delta_{\Gamma_{d_1}}[\![\mathbf{u}]\!]_1 \otimes \mathbf{n}_1\right)^s + \left(\delta_{\Gamma_{d_2}}[\![\mathbf{u}]\!]_2 \otimes \mathbf{n}_2\right)^s}_{\text{singular part}} \tag{15}$$

where, $\delta_{\Gamma_d} = \delta_{\Gamma_d}(\mathbf{x})$ is the Dirac's delta distribution appearing from the gradient of the Heaviside function, and $(\bullet)^s$ denotes the symmetric part of tensor $(\bullet)$. As it can be seen from Eq. (15), the strain field has a regular part which is bounded and a singular part which is unbounded.

Due to the singularity introduced by the Dirac functions in the strain field, it is not straightforward to define constitutive relationships. This comes from the fact that $\boldsymbol{\sigma}$ has to be bounded to satisfy the equilibrium even though $\boldsymbol{\epsilon}$ is unbounded. In the one crack case, one approach consists in deriving the discrete constitutive equations at the discontinuity level using the continuum constitutive law [36, 26, 37] which is termed as *Continuum Strong Discontinuity Approach* (CSDA). This is achieved by regularizing the Dirac's delta function using a collocation function defined on a band of finite width centered on Γ_d. In another approach, this problem can be solved by treating the crack as a discrete surface in the continuum [52, 53]. This is termed as *Discrete Strong Discontinuity Approach* (DSDA), which is followed in this work. The crack initiates when an assumed criterion is reached and the discrete constitutive law at the discontinuity is defined independently from the continuum constitutive law. From now on, the implicit dependence on $(\mathbf{x}, t)$ is omitted when no confusion is possible.

Augmented BVP. In a continuum mechanics context, the Boundary Value Problem (BVP) to be solved consists in finding the displacement field $\mathbf{u}$ which satisfies the equilibrium equations, compatibility conditions and constitutive relationship along with the given displacement and traction boundary conditions. However, in the presence of a strong discontinuity, the enhanced kinematics and the traction continuity conditions across the cracks need to be taken into account. Due to the principle of superposition invoked previously, the individual traction continuity conditions related to the discontinuities are coupled to obtain the local equilibrium of the superposed states. Hence, an augmented BVP is obtained as follows:

$$\begin{cases} \operatorname{div} \boldsymbol{\sigma} = 0 & \text{on } \mathcal{B} & \text{(16a)} \\ \boldsymbol{\epsilon} = \nabla^s \mathbf{u} & \text{on } \mathcal{B} & \text{(16b)} \\ \boldsymbol{\sigma} = \mathcal{F}(\boldsymbol{\epsilon}) & \text{on } \mathcal{B} & \text{(16c)} \\ \mathbf{u} = \mathbf{u}_0 & \text{on } \partial_u \mathcal{B} & \text{(16d)} \\ \boldsymbol{\sigma} \cdot \mathbf{p} = \mathbf{t}_0 & \text{on } \partial_t \mathcal{B} & \text{(16e)} \\ \boldsymbol{\sigma} \cdot \mathbf{n}_1 = \mathbf{t}_1 & \text{on } \Gamma_{d_1} & \text{(16f)} \\ \boldsymbol{\sigma} \cdot \mathbf{n}_2 = \mathbf{t}_2 & \text{on } \Gamma_{d_2} & \text{(16g)} \\ \mathbf{t}_1 = h_1([\![\mathbf{u}]\!]_1) & \text{on } \Gamma_{d_1} & \text{(16h)} \\ \mathbf{t}_2 = h_2([\![\mathbf{u}]\!]_2) & \text{on } \Gamma_{d_2} & \text{(16i)} \end{cases}$$

where, $\operatorname{div}(\bullet)$ denotes the divergence operator, $\mathcal{F}$ denotes a constitutive relation between $\boldsymbol{\sigma}$ and $\boldsymbol{\epsilon}$, $(\mathbf{t}_1, \mathbf{t}_2)$ are the traction vectors on the discontinuities surface, (h_1, h_2) are the discrete constitutive laws, and $(\mathbf{t}_0, \mathbf{u}_0)$ are applied traction and displacement respectively. Finally, $\partial_t \mathcal{B} \subset \partial \mathcal{B}$ and $\partial_u \mathcal{B} \subset \partial \mathcal{B}$ are the parts of the boundary such that $\partial_t \mathcal{B} \cup \partial_u \mathcal{B} = \mathcal{B}$ and $\partial_t \mathcal{B} \cap \partial_u \mathcal{B} = \emptyset$.

3.2. Embedded finite element method

The Hu-Washizu variational principle [54] is considered to derive the weak formulation. Since the displacement jumps are embedded inside a finite element, the enhanced assumed strains of both cracks are treated locally.

3.2.1. Enhanced assumed strain method

Variational form of the augmented BVP. In the Enhanced Assumed Strain (EAS) method, the enhanced kinematics of the continuum is taken into account by representing the discontinuous parts of the strain field as enhanced strains $(\tilde{\boldsymbol{\epsilon}})$ as follows:

$$\boldsymbol{\epsilon} = \nabla^s \mathbf{u} + \tilde{\boldsymbol{\epsilon}}_1 + \tilde{\boldsymbol{\epsilon}}_2 \tag{17}$$

Let us denote $(\mathbf{u}^*, \boldsymbol{\epsilon}^*, \tilde{\boldsymbol{\sigma}}^*)$ the virtual variations corresponding to $(\mathbf{u}, \boldsymbol{\epsilon}, \tilde{\boldsymbol{\sigma}})$. The three-fields variational

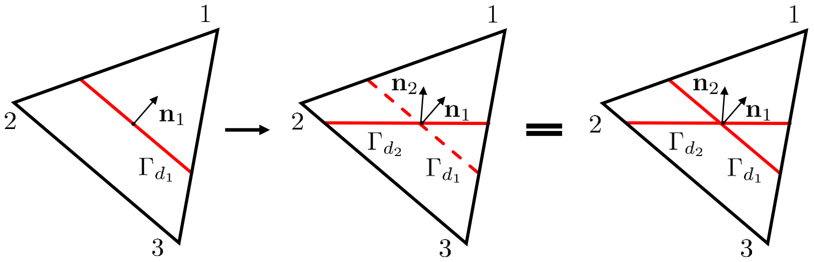

Figure 3: Augmented E-FEM - a finite element ($\mathcal{B}_e^h \in \mathcal{E}_1 \cap \mathcal{E}_2$) with multiple intersecting discontinuities Γ_{d_1} and Γ_{d_2}

problem to be solved consist in finding $(\mathbf{u}, \boldsymbol{\epsilon}, \tilde{\boldsymbol{\sigma}}) \in (\mathsf{U}, \mathsf{E}, \mathsf{S})$ such that $\forall\ (\mathbf{u}^*, \boldsymbol{\epsilon}^*, \tilde{\boldsymbol{\sigma}}^*) \in (\mathsf{U}_0, \mathsf{E}, \mathsf{S})$,

$$\int_{\mathcal{B}} \nabla^s(\mathbf{u}^*) : \boldsymbol{\sigma}(\boldsymbol{\epsilon})\ dV - \int_{\partial_t \mathcal{B}} \mathbf{u}^* \cdot \mathbf{t}_0\ dS = 0 \tag{18}$$

$$\int_{\mathcal{B}} \tilde{\boldsymbol{\sigma}}^* : \left[\nabla^s \mathbf{u} - \boldsymbol{\epsilon}\right]\ dV = 0 \tag{19}$$

$$\int_{\mathcal{B}} \boldsymbol{\epsilon}^* : \left[-\tilde{\boldsymbol{\sigma}} + \boldsymbol{\sigma}(\boldsymbol{\epsilon})\right]\ dV = 0 \tag{20}$$

where $\boldsymbol{\sigma}(\boldsymbol{\epsilon})$ is the stress in the continuum defined by the constitutive law Eq. (16c). The admissibility set U and spaces U_0, E and S are defined as $\mathsf{U} = \left\{\mathbf{u} | \mathbf{u} \in H^1(\mathcal{B}), \mathbf{u} = \mathbf{u}_0 \text{ on } \partial_u \mathcal{B}\right\}$, $\mathsf{U}_0 = \left\{\mathbf{u} | \mathbf{u} \in H_0^1(\mathcal{B}), \mathbf{u} = 0 \text{ on } \partial_u \mathcal{B}\right\}$, $\mathsf{E} = \left\{\boldsymbol{\epsilon} | \boldsymbol{\epsilon} \in \mathcal{L}^2(\mathcal{B})\right\}$ and $\mathsf{S} = \left\{\tilde{\boldsymbol{\sigma}} | \tilde{\boldsymbol{\sigma}} \in \mathcal{L}^2(\mathcal{B})\right\}$, where $H^1(\mathcal{B})$ and $H_0^1(\mathcal{B})$ are homogeneous first-order Sobolev spaces on $\mathcal{B}$ respectively. $\mathcal{L}^2(\mathcal{B})$ denotes the set of square-integrable functions on $\mathcal{B}$. Let us note that $\boldsymbol{\sigma}$ and $\tilde{\boldsymbol{\sigma}}$ are both stress fields. However, $\boldsymbol{\sigma}$ is assumed to fulfill the constitutive law equations whereas $\tilde{\boldsymbol{\sigma}}$ fulfills static admissibility condition.

Finite element approximation. Now, let us consider the finite element discretization $\mathcal{B}^h \subset \mathcal{B}$, composed by n_{elem} non-overlapping finite elements $\mathcal{B}_e^h$ such that $\mathcal{B}^h = \cup_{e=1}^{n_{elem}} \mathcal{B}_e^h$. In general, the inter element continuity is not ensured on the stress and strain fields which allows to introduce the required enhancements locally in a finite element. Hence, the corresponding discretized displacement field consists of the nodal DOFs ($\mathbf{d}$) and the elemental enhanced displacement fields ($\mathbf{e}_1$, $\mathbf{e}_2$).

Let $\mathcal{E}_1^h$ and $\mathcal{E}_2^h$ denote the set of finite elements that are crossed by the Γ_{d_1} and Γ_{d_2} respectively. In case of multiple intersecting cracks, $\mathcal{E}_1 \cap \mathcal{E}_2$ is not an empty set. Here, we use Constant Strain Triangular (CST) elements, in which two intersecting cracks are initiated at the single Gauss integration point at the centroid of the element. Let us consider that Γ_{d_1} and Γ_{d_2} divide the finite elements $\mathcal{B}_e^{h_1} \in \mathcal{E}^{h_1}$ and $\mathcal{B}_e^{h_2} \in \mathcal{E}^{h_2}$ into sub-domains $(\mathcal{B}_e^{h_1})^+$, $(\mathcal{B}_e^{h_1})^-$ and $(\mathcal{B}_e^{h_2})^+$, $(\mathcal{B}_e^{h_2})^-$ respectively such that $\mathbf{n}_1$ and $\mathbf{n}_2$ are inward $(\mathcal{B}_e^{h_1})^-$ and $(\mathcal{B}_e^{h_2})^-$ respectively (Fig. 3).

The finite element approximation of $\mathbf{u}$ is constructed as:

$$\mathbf{u} = \mathbf{N}_a \mathbf{d} + \mathbf{N}_{c_1} \mathbf{e}_1 + \mathbf{N}_{c_2} \mathbf{e}_2 \tag{21}$$

where, $\mathbf{N}_a$ denotes the elementary shape functions matrix, $\mathbf{N}_{c_1} = \mathbf{H}_{\Gamma_{d_1}} - \sum_{a \in (\mathcal{B}_e^{h_1})^+} \mathbf{N}_a$ and $\mathbf{N}_{c_2} = \mathbf{H}_{\Gamma_{d_2}} - \sum_{a \in (\mathcal{B}_e^{h_2})^+} \mathbf{N}_a$ are the shape functions matrices for the enhanced displacement fields [25, 21]. Here, $\mathbf{H}_{\Gamma_{d_1}}$ and $\mathbf{H}_{\Gamma_{d_2}}$ stand for the matrices formed using the Heaviside function. For the sake of clarity, we remove the subscript a for the nodal DOFs and interpolation functions.

The approximation of the variational field $\mathbf{u}^*$ is the same approximation of $\mathbf{u}$ (Eq. (21)). The approximations of the strain and its virtual field can be constructed in different ways depending on the type of discontinuity and the chosen method for fulfillment of traction continuity condition as described in [55, 56]. In the formulation termed as *Statically Optimal Symmetric* (SOS), the traction continuity condition is satisfied while the kinematics of strong discontinuity is not well represented. In contrast to this, *Kinematically Optimal Symmetric* (KOS) formulation represents kinematics of strong discontinuity correctly but equilibrium across the cracks is not ensured in complex deformation modes.

Here, we follow *Statically and Kinematically Optimal Nonsymmetric* (SKON) formulation which takes into account both the kinematics of strong discontinuity and the traction continuity in a well manner. In this formulation, the strain interpolation is performed using the gradient matrices of $\mathbf{N}_{c_1}$, $\mathbf{N}_{c_2}$ for $\boldsymbol{\epsilon}$. Another matrix constructed from the functions that satisfies the zero mean over the finite element is chosen for the virtual strain field. Thus, the finite element approximations of $\boldsymbol{\epsilon}$, $\boldsymbol{\epsilon}^*$ are obtained as:

$$\boldsymbol{\epsilon} = \mathbf{B}\mathbf{d} + \mathbf{G}_1\mathbf{e}_1 + \mathbf{G}_2\mathbf{e}_2 \quad \text{and} \quad \boldsymbol{\epsilon}^* = \mathbf{B}\mathbf{d}^* + \mathbf{G}_1^*\mathbf{e}_1^* + \mathbf{G}_2^*\mathbf{e}_2^* \tag{22}$$

where, $\mathbf{B}$ is the standard strain-displacement matrix (i.e., the gradient matrix of $\mathbf{N}$) and $\mathbf{G}_1$, $\mathbf{G}_2$ and $\mathbf{G}_1^*$ $\mathbf{G}_2^*$ are the interpolation matrices of the enhanced strains and their virtual counterparts given by:

$$\mathbf{G}_1 = \mathbf{P}_1\delta_{\Gamma_{d_2}} - \sum_{a\in(\mathcal{B}_e^{h2})^+} \mathbf{B}_a \quad \text{and} \quad \mathbf{G}_2 = \mathbf{P}_2\delta_{\Gamma_{d_1}} - \sum_{a\in(\mathcal{B}_e^{h1})^+} \mathbf{B}_a \tag{23}$$

$$\mathbf{G}_1^* = \left(\delta_{\Gamma_{d_1}} - \frac{\text{meas}(\Gamma_d)}{\text{meas}(\mathcal{B}_e^{h_1})}\right)\mathbf{P}_1 \quad \text{and} \quad \mathbf{G}_2^* = \left(\delta_{\Gamma_{d_2}} - \frac{\text{meas}(\Gamma_d)}{\text{meas}(\mathcal{B}_e^{h_2})}\right)\mathbf{P}_2 \tag{24}$$

with the projection matrices defined at the discontinuity surface as:

$$\mathbf{P}_1 = \begin{bmatrix} n_{1_1} & 0 \\ 0 & n_{1_2} \\ n_{1_2} & n_{1_1} \end{bmatrix} \quad \text{and} \quad \mathbf{P}_2 = \begin{bmatrix} n_{2_1} & 0 \\ 0 & n_{2_2} \\ n_{2_2} & n_{2_1} \end{bmatrix} \tag{25}$$

where, $[n_{1_1}, n_{1_2}]$, $[n_{2_1}, n_{2_2}]$ are the components of $\mathbf{n}_1$ and $\mathbf{n}_2$ respectively in the orthonormal basis $R(\mathbf{x}_1, \mathbf{x}_2)$, and meas($\bullet$) representing the measure of ($\bullet$). In this manner, both the kinematics of strong discontinuity and the traction continuity are represented in a well manner.

As we use CST elements, the traction is constant across the element. We then substitute Eqs. (23) and (24) in Eqs. (18) to (20) and use the zero mean property of $\mathbf{G}^*$ [3] to obtain the following final global and local equilibrium equations (using the assembly operator A):

$$\begin{cases} \overset{n_{elem}}{\underset{e=1}{\mathsf{A}}} \displaystyle\int_{\mathcal{B}_e} \mathbf{B}^\top \boldsymbol{\sigma}(\mathbf{B}\mathbf{d} + \mathbf{G}_1\mathbf{e}_1 + \mathbf{G}_2\mathbf{e}_2)\ dV = \mathbf{F}_{ext} & \text{(26a)} \\ \mathbf{t}_1(\mathbf{e}_1) - \dfrac{1}{\text{meas}(\mathcal{B}_e^{h_1})} \displaystyle\int_{\mathcal{B}_e^{h_1}} \mathbf{P}_1^\top \boldsymbol{\sigma}(\mathbf{B}\mathbf{d} + \mathbf{G}_1\mathbf{e}_1 + \mathbf{G}_2\mathbf{e}_2)\ dV = 0 \quad \forall\ \mathcal{B}_e^{h_1} \in \mathcal{E}_1 & \text{(26b)} \\ \mathbf{t}_2(\mathbf{e}_2) - \dfrac{1}{\text{meas}(\mathcal{B}_e^{h_2})} \displaystyle\int_{\mathcal{B}_e^{h_2}} \mathbf{P}_2^\top \boldsymbol{\sigma}(\mathbf{B}\mathbf{d} + \mathbf{G}_1\mathbf{e}_1 + \mathbf{G}_2\mathbf{e}_2)\ dV = 0 \quad \forall\ \mathcal{B}_e^{h_2} \in \mathcal{E}_2 & \text{(26c)} \end{cases}$$

where, $\mathbf{F}_{ext} = \int_{\partial_t \mathcal{B}} \mathbf{N}^\top \mathbf{t}_0\ dS$ is the standard external force vector.

3.3. Numerical resolution

In this section the numerical resolution of the governing equilibrium equations is presented. Eqs. (26a) to (26c) are solved in a incremental iterative manner using modified Newton method. Similar to the standard E-FEM [52, 53], static condensation procedure can be applied (Eqs. (26a) to (26c)). Then, the so called operator split method is used for solving the global and local equilibrium equations in a staggered manner.

---

[3] For a given function $z(\mathbf{x})$ defined on $\mathcal{B}$, the property $\int_{\mathcal{B}} \delta_{\Gamma_d} z(\mathbf{x})\ dV = \int_{\Gamma_d} z_{\Gamma_d}\ dS$ holds true. Here, z_{Γ_d} is the value of the function on the discontinuity.

3.3.1. Incremental iterative scheme

The pseudo-time domain is discretized according to a sequence of N pseudo-time instants $\{t^n\}_{n=1}^{N}$ such that $t^{n+1} = t^n + \Delta t$, with Δt standing for a pseudo-time step. The evolution of the external loading is then applied incrementally ($\Delta\mathbf{F}_{ext}^{n+1}$) with respect to the discretized pseudo-time t^{n+1} as, $\mathbf{F}_{ext}^{n+1} = \mathbf{F}_{ext}^{n} + \Delta\mathbf{F}_{ext}^{n+1}$. Here, we apply a displacement-controlled loading and the boundary conditions are enforced using a double Lagrange multiplier technique [57, 58]. Then, the unknown increments $\Delta\mathbf{s}^{n+1} = (\Delta\mathbf{d}^{n+1}, \Delta\mathbf{e}_1^{n+1}, \Delta\mathbf{e}_2^{n+1})$ are obtained by solving the discrete system of Eqs. (26a) to (26c), for the given $\Delta\mathbf{F}_{ext}^{n+1}$, and the solution at t^{n+1} is updated as, $\mathbf{s}^{n+1} = \mathbf{s}^n + \Delta\mathbf{s}^{n+1}$, where $\mathbf{s}^n = (\mathbf{d}^n, \mathbf{e}_1^n, \mathbf{e}_2^n)$ is the solution at time t^n. The Eqs. (26a) to (26c) being non-linear, the increments of the solution fields are obtained using an iterative procedure. In this work, we adopt a modified Newton method for each pseudo-time step. The solution increments at iteration $i+1$ at time increment t^{n+1} are obtained as, $\Delta\mathbf{s}^{n+1,i+1} = \Delta\mathbf{s}^{n+1,i} + \delta\mathbf{s}^{n+1,i+1}$. Here, $\delta\mathbf{s}^{n+1,i+1} = (\delta\mathbf{d}^{n+1,i+1}, \delta\mathbf{e}_1^{n+1,i+1}, \delta\mathbf{e}_1^{n+1,i+1})$ is the solution increment between iterations i and $i+1$ whereas $\Delta\mathbf{s}^{n+1,i} = (\Delta\mathbf{d}^{n+1,i}, \Delta\mathbf{e}_1^{n+1,i}, \Delta\mathbf{e}_2^{n+1,i})$ is the solution variation at iteration i.[4]

In order to obtain $\left(\delta\mathbf{d}^{i+1}, \delta\mathbf{e}_1^{i+1}, \delta\mathbf{e}_2^{i+1}\right)$, we define the residuals of the global and local equilibrium equations at iteration $i+1$ as follows:

$$\begin{cases}
\mathbf{R}(\mathbf{d}^{i+1}, \mathbf{e}_1^{i+1}, \mathbf{e}_2^{i+1}) = \mathbf{F}_{ext} - \mathop{\mathsf{A}}\limits_{e=1}^{n_{elem}} \displaystyle\int_{\mathcal{B}_e} \mathbf{B}^{\top} \boldsymbol{\sigma}(\mathbf{d}^{i+1}, \mathbf{e}_1^{i+1}, \mathbf{e}_2^{i+1})\; dV & (27a) \\
\mathbf{r}_1(\mathbf{d}^{i+1}, \mathbf{e}_1^{i+1}, \mathbf{e}_2^{i+1}) = \mathbf{t}_1(\mathbf{e}_1^{i+1}) - \dfrac{1}{\mathrm{meas}(\mathcal{B}_e^{h_1})} \displaystyle\int_{\mathcal{B}_e^{h_1}} \mathbf{P}^{\top} \boldsymbol{\sigma}(\mathbf{d}^{i+1}, \mathbf{e}_1^{i+1}, \mathbf{e}_2^{i+1})\; dV \quad \forall\, \mathcal{B}_e^{h_1} \in \mathcal{E}_1 & (27b) \\
\mathbf{r}_2(\mathbf{d}^{i+1}, \mathbf{e}_1^{i+1}, \mathbf{e}_2^{i+1}) = \mathbf{t}_2(\mathbf{e}_2^{i+1}) - \dfrac{1}{\mathrm{meas}(\mathcal{B}_e^{h_2})} \displaystyle\int_{\mathcal{B}_e^{h_2}} \mathbf{P}^{\top} \boldsymbol{\sigma}(\mathbf{d}^{i+1}, \mathbf{e}_1^{i+1}, \mathbf{e}_2^{i+1})\; dV \quad \forall\, \mathcal{B}_e^{h_2} \in \mathcal{E}_2 & (27c)
\end{cases}$$

Now, we minimize the residuals at the iteration $i+1$ using the solution $(\mathbf{d}^i, \mathbf{e}_1^i, \mathbf{e}_2^i)$ at iteration i to obtain the linearized system of the global and local equilibrium equations:

$$\begin{cases}
\mathbf{K}_{bb}^{i}\delta\mathbf{d}^{i+1} + \mathbf{K}_{bg_1}^{i}\delta\mathbf{e}_1^{i+1} + \mathbf{K}_{bg_2}^{i}\delta\mathbf{e}_2^{i+1} = \mathbf{F}_{ext} - \mathbf{F}_{int}^{i} & (28a) \\
\mathbf{K}_{g_1 b}^{i}\delta\mathbf{d}^{i+1} + \mathbf{K}_{g_1 g_1}^{i}\delta\mathbf{e}_1^{i+1} + \mathbf{K}_{g_1 g_2}^{i}\delta\mathbf{e}_2^{i+1} = (\mathbf{f}_1)_{int}^{i} \quad \forall\, \mathcal{B}_e^{h_1} \in \mathcal{E}_1 & (28b) \\
\mathbf{K}_{g_2 b}^{i}\delta\mathbf{d}^{i+1} + \mathbf{K}_{g_2 g_1}^{i}\delta\mathbf{e}_1^{i+1} + \mathbf{K}_{g_2 g_2}^{i}\delta\mathbf{e}_2^{i+1} = (\mathbf{f}_2)_{int}^{i} \quad \forall\, \mathcal{B}_e^{h_2} \in \mathcal{E}_2 & (28c)
\end{cases}$$

---

[4] From here-forth, the dependency on the time step is skipped for the sake of conciseness when no confusion is possible. As a consequence, every quantity without the superscript $n+1$ has to be intended as referred to t^{n+1}.

where, (with $\bullet, \bullet\bullet = 1, 2$):

$$\mathbf{F}^i_{int} = \mathop{\mathsf{A}}_{e=1}^{n_{elem}} \int_{\mathcal{B}_e} \mathbf{B}^\top \boldsymbol{\sigma}(\mathbf{d}^i, \mathbf{e}^i_1, \mathbf{e}^i_2)\; dV \tag{29}$$

$$\mathbf{K}^i_{bb} = \mathop{\mathsf{A}}_{e=1}^{n_{elem}} \int_{\mathcal{B}^{h_1}_e} \mathbf{B}^\top \mathbf{C}\mathbf{B}\; dV, \tag{30}$$

$$\mathbf{K}^i_{bg_\bullet} = \int_{\mathcal{B}^{h_1}_e} \mathbf{B}^\top \mathbf{C}\mathbf{G}_r\; dV, \tag{31}$$

$$\mathbf{K}^i_{g_\bullet b} = -\frac{1}{\mathrm{meas}(\mathcal{B}^{h_\bullet}_e)} \int_{\mathcal{B}^{h_\bullet}_e} \mathbf{P}^\top_\bullet \mathbf{C}\mathbf{B}\; dV, \tag{32}$$

$$\mathbf{K}^i_{g_\bullet g_\bullet} = \left.\frac{\partial \mathbf{t}_\bullet}{\partial \mathbf{e}_\bullet}\right|_{\mathbf{e}^i_\bullet} - \frac{1}{\mathrm{meas}(\mathcal{B}^{h_\bullet}_e)} \int_{\mathcal{B}^{h_\bullet}_e} \mathbf{P}^\top_\bullet \mathbf{C}\mathbf{G}_r\; dV, \tag{33}$$

$$\mathbf{K}^i_{g_\bullet g_{\bullet\bullet}} = -\frac{1}{\mathrm{meas}(\mathcal{B}^{h_\bullet}_e)} \int_{\mathcal{B}^{h_\bullet}_e} \mathbf{P}^\top_\bullet \mathbf{C}\mathbf{G}_{\bullet\bullet}\; dV \tag{34}$$

$$(\mathbf{f}_\bullet)^i_{int} = \mathbf{t}_r\left(\mathbf{e}^i_\bullet\right) - \frac{1}{\mathrm{meas}(\mathcal{B}^{h_\bullet}_e)} \int_{\mathcal{B}^{h_\bullet}_e} \mathbf{P}^\top_\bullet \boldsymbol{\sigma}\left(\boldsymbol{\epsilon}^i\right)\; dV \tag{35}$$

The numerical experience showed that choosing the elastic tensor as the iteration operator led to a robust convergence. This explains why the elastic tensor $\mathbf{C}$ is used in the softening regime. Moreover, the stiffness matrices $\mathbf{K}^i_{g_1 g_2}$ and $\mathbf{K}^i_{g_2 g_1}$ have non-zero stiffness terms only if both $\mathcal{B}^{h_1}_e$ and $\mathcal{B}^{h_2}_e$ belong to $\mathcal{E}_1 \cap \mathcal{E}_2$. In other words, for the elements in which the two cracks intersect, the coupled traction-separation laws are solved. In the elements that contain only the first crack, we solve the system of equations related to only a single crack.

Here, the static condensation can be performed at the element level to eliminate DOFs corresponding to $\mathbf{e}^i_1$ and $\mathbf{e}^i_2$ from the global DOFs. This allows obtaining the following modified system of equations:

$$\tilde{\mathbf{K}}^i \delta\mathbf{d}^{i+1} = \mathbf{F}_{ext} - \tilde{\mathbf{F}}^i_{int} \tag{36}$$

where:

$$\tilde{\mathbf{K}}^i = \mathbf{K}^i_{bb} - \mathbf{K}^i_{bg_1}\left[\mathbf{K}^i_{g_1 g_1}\right]^{-1}\mathbf{K}^i_{g_1 b} - \mathbf{K}^i_{bg_2}\left[\mathbf{K}^i_{g_2 g_2}\right]^{-1}\mathbf{K}^i_{g_2 b} \tag{37}$$

$$\tilde{\mathbf{F}}^i_{int} = \mathbf{F}^i_{int} - \mathbf{K}^i_{bg_1}\left[\mathbf{K}^i_{g_1 g_1}\right]^{-1}(\mathbf{f}_1)^i_{int} - \mathbf{K}^i_{bg_2}\left[\mathbf{K}^i_{g_2 g_2}\right]^{-1}(\mathbf{f}_2)^i_{int} \tag{38}$$

3.3.2. Staggered solution scheme: operator split method

The solution of the linearized system of equations Eqs. (28a) to (28c) is obtained in a staggered manner. In other words, the solution of the global equilibrium at the iteration $i+1$ is obtained first using the solution of the local equilibrium at previous iteration i and second the residual of the local equilibrium is redefined taking into account the global solution at the iteration $i+1$. This procedure is known as *operator split method* which is described in detail here.

Global equilibrium equation. The residual of the global equilibrium Eq. (26a) is redefined as, $\mathbf{R}(\mathbf{d}^{i+1}, \mathbf{e}^i_1, \mathbf{e}^i_2) = 0$. Since $\mathbf{e}^i_1$ and $\mathbf{e}^i_2$ are known, the static condensation can be performed and the solution $\delta\mathbf{d}^{i+1}$ of Eq. (36) is obtained.

Coupled Local equilibrium equations. The residuals of the coupled traction continuity conditions Eqs. (26b) and (26c) is redefined using $\delta\mathbf{d}^{i+1}$. Since these equations are also non-linear, an iterative procedure is used at the local level to compute $\delta\mathbf{e}_1^{i+1}$ and $\delta\mathbf{e}_2^{i+1}$. At local iteration $j+1$, one solves the following problem:

$$\begin{cases} \mathbf{r}_1(\mathbf{d}^{i+1}, \mathbf{e}_1^{j+1}, \mathbf{e}_2^{j+1}) = \mathbf{r}_1(\mathbf{d}^{i}, \delta\mathbf{d}^{i+1}, \mathbf{e}_1^{j}, \mathbf{e}_2^{j}) + \mathbf{K}^j_{g_1g_1}\delta\mathbf{e}_1^{j+1} + \mathbf{K}^j_{g_1g_2}\delta\mathbf{e}_2^{j+1} = 0 & \text{(39a)} \\ \mathbf{r}_2(\mathbf{d}^{i+1}, \mathbf{e}_1^{j+1}, \mathbf{e}_2^{j+1}) = \mathbf{r}_2(\mathbf{d}^{i}, \delta\mathbf{d}^{i+1}, \mathbf{e}_1^{j}, \mathbf{e}_2^{j}) + \mathbf{K}^j_{g_2g_1}\delta\mathbf{e}_1^{j+1} + \mathbf{K}^j_{g_2g_2}\delta\mathbf{e}_2^{j+1} = 0 & \text{(39b)} \end{cases}$$

The discretized displacement jumps at $j+1$ are then obtained as, $\mathbf{e}_1^{j+1} = \mathbf{e}_1^{j} + \delta\mathbf{e}_1^{j+1}$ and $\mathbf{e}_2^{j+1} = \mathbf{e}_2^{j} + \delta\mathbf{e}_2^{j+1}$. Now, once the local convergence is achieved $\mathbf{e}_1^{i+1}$, $\mathbf{e}_2^{i+1}$ are set equal to $\mathbf{e}_1^{j+1}$, $\mathbf{e}_2^{j+1}$. The residual at the iteration $i+1$ is then updated as $\mathbf{R}(\mathbf{d}^{i+1}, \mathbf{e}_1^{i+1}, \mathbf{e}_2^{i+1})$, which is checked for a given tolerance ($||\mathbf{R}|| \leq 10^{-6}$). As an advantage of the operator split method, the terms $\mathbf{f}^i_{int}$ appearing in Eq. (36) are null during the local solving. Thus, the internal force vector is formed only by the global forces coming from the stresses in the bulk. The above methodology is implemented in CastLab [58], an in-house FE code in MATLAB® environment.

Traction-separation law. Following [59], a constitutive law on the discontinuity can be defined within the framework of thermodynamics of irreversible processes using an isotropic damage-like internal variable d_{cr}. The latter represents the degradation of the cohesive properties related to the discontinuity. The Helmholtz free energy is introduced as a surface energy density, $\psi_S = \psi_S([\![\mathbf{u}]\!], d_{cr})$. It represents the available energy density for the formation of crack is thus written as $\psi_S = (1/2)(1-d_{cr})[\![\mathbf{u}]\!] \cdot \mathbf{K} \cdot [\![\mathbf{u}]\!]$, where, $\mathbf{K}$ stands for the stiffness operator. The traction-separation law which is given in terms of $\mathbf{t}$ and $[\![\mathbf{u}]\!]$ at Γ_d as:

$$\mathbf{t} = \frac{\partial \psi_S}{\partial [\![\mathbf{u}]\!]} = (1-d_{cr})\ \mathbf{K} \cdot [\![\mathbf{u}]\!] \tag{40}$$

In order to model both crack opening and sliding, a mixed mode traction-separation law is considered. Following the proposal made by [59], the expression of d_{cr} is given in terms of the fracture energy ($G_{f,S}$) and κ_{cr}, an internal (history) variable which is defined using the historical maxima of $[\![u]\!]_n$ and $[\![u]\!]_s$:

$$d_{cr} = 1 - \frac{\kappa^0_{cr}}{\kappa_{cr}} \exp\left(-\frac{f_t}{G_{f,S}}\left(\kappa_{cr} - \kappa^0_{cr}\right)\right) \quad \text{with} \quad \kappa_{cr} = \max\langle [\![u]\!]_n\rangle^+ + \beta_{cr} \max|[\![u]\!]_s| \tag{41}$$

where, $\beta_{cr} \leq 1$ is a model parameter allowing to weight the mode-I with respect to the mode-II and κ^0_{cr} is a non-zero value of the internal variable at the crack initiation. The stiffness tensor is then considered as [59], $\mathbf{K} = f_t/\kappa^0_{cr}\boldsymbol{I}$, where, $\boldsymbol{I}$ is the second-order identity tensor. Here, κ^0_{cr} ensures a smooth evolution of d_{cr} which ranges between 0 (no crack) and 1 (fully opened cohesive crack). Finally, the yield surface, $f_{cr} = f_{cr}([\![u]\!]_n, [\![u]\!]_s, \kappa_{cr})$, and the loading-unloading (Kuhn-Tucker) conditions are given as:

$$f_{cr} = \langle [\![u]\!]_n\rangle^+ + \beta_{cr}|[\![u]\!]_s| - \kappa_{cr} = 0 \quad \text{and} \quad \dot{\kappa}_{cr} \geq 0,\ f_{cr} \leq 0,\ \dot{\kappa}_{cr} f_{cr} = 0 \tag{42}$$

4. Microplane microdamage model to strong discontinuity: transition approach

The transition models' purpose is to describe the energy dissipation occurring at both the localized damage zone and the crack in a coupled manner. A transition framework is used such that the energy which is to be dissipated by the coupled model (sum of the volumetric and surface parts) is equivalent to the energy which is to be dissipated by the microplane model without transition. Following the energy equivalence approach proposed in [34], the total energy dissipated by microplane and strong discontinuity models is equivalent.

4.1. Single crack formulation

From a phenomenological point of view, the crack is formed inside a given localization zone. Hence, the energy dissipated during the strain localization process can be divided into two parts: (i) the volumetric part that accounts for the formation and growth of a damaged/localization band (described though a continuum model, a microplane model in the present case); (ii) the surface part that accounts for the initiation and propagation of the crack (described through a strong discontinuity model, in the present case). In this section, we present the formulation of microplane microdamage model to strong discontinuity model transition approach by considering that a single crack is initiated during the second phase of strain localization.

4.1.1. Formulation

The transition approach is presented by enforcing the energy equivalence in a weak form [60], that is to say, by considering the energy dissipation of the uncoupled and coupled models over entire pseudo-time domain (loading history)[5]. Within the context of the transition approach, before the transition pseudo-time (t_{tr}), there is a part of total energy dissipated in the unit volume, and a part dissipated on the crack surface after the transition. Therefore, in the case of the microplane model, we have:

$$\underbrace{\int_{\mathcal{B}}\int_0^{\infty}\dot{\phi}_V\,dt\,dV}_{:=\phi_V}=\int_{\mathcal{B}}\underbrace{\int_0^{t_{\mathrm{tr}}}\frac{1}{\pi}\int_{\Omega}\dot{\phi}_V^{\alpha}\,dS\,dt}_{:=\hat{\phi}_V}\,dV+\int_{\Gamma_d}\underbrace{\int_{t_{\mathrm{tr}}}^{\infty}\dot{\phi}_S\,dt}_{:=\hat{\phi}_S}\,d\Gamma \tag{43}$$

Following Eq. (43), the energy available for the crack formation is obtained as the difference between the energy which is to be dissipated by the microplane microdamage model without transition and the energy already dissipated in the localization band before transition. Using Eq. (11) for the relation between the density of energy dissipation in a unit volume and its microplane counterpart, one has:

$$\phi_S=\int_{\Gamma_d}\hat{\phi}_S\,d\Gamma=\int_{\mathcal{B}}\left(g_f-\hat{\phi}_V\right)\,dV=\frac{1}{\pi}\int_{\mathcal{B}}\int_{\Omega}\left(g_f^{\pi}-\hat{\phi}_V^{\alpha}\right)\,dS\,dV \tag{44}$$

Thus, the term $(g_f^{\pi}-\hat{\phi}_V^{\alpha})$ gives the residual energy on each microplane at the moment of transition. Due to the anisotropic nature of the microplane microdamage model, the residual energy is calculated as a directional dependent quantity.

In the previous equations Eqs. (43) and (44), we assumed that the energy dissipation in the bulk material stops once a crack is localized due to progressive unloading in the neighborhood of the crack. According to this approach, before the transition, the rate of the surface energy dissipation is equal to zero (a crack does not exist), and the increment of the energy dissipation in the bulk material is equal to the increment of the energy dissipation of the microplane model. After the transition, the energy dissipation rate in the bulk is equal to zero due to unloading in the band and the increment of the surface energy dissipation.

After an assumed criterion is fulfilled, the cohesive crack is introduced as a strong discontinuity in the maximum principal stress direction. Note that, in transition models [33, 62], the criterion for crack initiation is formulated based on the quantities at the unit volume or the internal variables. In the present work, transition criteria can be formulated based on quantities related to the microplanes (.g., $\tilde{\epsilon}^{\alpha}$, ω^{α}, and $\hat{\phi}_V^{\alpha}$), to exploit the anisotropic damage description provided by the microplane model.

Following the same approach as in [35, 63], the available energy computed from Eq. (44) is used to identify the parameters of the cohesive law.The parameters of the exponential traction-separation law (Eq. (40) and Eq. (41)), are then taken proportional to the available energy (i.e., $G_{f,S}\propto\hat{\phi}_S$), and the value of the maximum principal stress (σ_I) at the transition (i.e., $f_t=(\sigma_I)_{\mathrm{tr}}$) respectively.

---

[5] On contrary, the energy equivalence can be imposed in a strong sense by imposing it at each pseudo-time step [61]. However, this is less straight forward in the present case due to the complex integrals of the microplane model.

4.1.2. Algorithm

We focus on the formation of a single crack. This algorithm is presented for a given iteration $i+1$ at the present time step t^{n+1}. A Boolean variable $flag$, which is initiated with 0, is used to store the information of the crack opening activation. As soon as the crack is activated, $flag$ is set to 1.

The steps followed for the initiation and propagation of crack after transition are described below:

1. at a given Gauss point, compute the microplane quantities using the discretized fields $\mathbf{d}^{i+1}$ and $\mathbf{e}^{i}$ (initiated with $\mathbf{0}$). So, ϵ_m^α and ϵ_l^α are computed by projecting the total strain $(\mathbf{B}\mathbf{d}^{i+1}+\mathbf{G}\mathbf{e}^{i})$ on the microplanes (see Eq. (1)).
2. if the crack is not activated in the previous time step (i.e., $flag = 0$) then the transition criterion is checked. Here, two cases can be distinguished:
    (a) if the transition criterion is not fulfilled, the microdamage variable and the energy dissipation are updated.
    (b) if the transition criterion is fulfilled on at least one microplane, then the crack is activated. Using the energy regularization technique (see Section 2.3), the energy available for the crack is obtained as[6]:

    $$G_{f,S} = \hat{\phi}_S = \frac{1}{\pi}\left(\sum_{\Omega^\alpha}(g_f^\pi - \hat{\phi}_V^\alpha)W^\alpha\right) l_c \tag{45}$$

    The traction continuity condition is then solved according to E-FEM.

Note that, while solving the local equilibrium equation using the operator split method, the stress tensor in the bulk needs to be updated during the iterations. During the solution procedure of the local traction continuity condition, the microdamage variables are frozen to avoid any instabilities at the local level, due to the concurrent correction of the microdamage distribution and crack-opening at the strong discontinuity level.

4.2. Multiple crack formulation

In this section, we extend the proposed transition framework for describing the formation of multiple intersecting orthogonal and non-orthogonal cracks. In particular, we capture the anisotropic damage growth due to the rotation of the principal stress/strain axes during loading and benefit from information provided by the microplane formulation to initiate multiple cracks. Please note that one can handle the principal stress/strain axes rotation by considering a complex traction-separation law at a single discontinuity. However, we choose this path because our objective is to model multiple intersecting cracks, for example, in the case of a shear cyclic loading.

4.2.1. Formulation

Let us consider a unit volume submitted to complex loading conditions such that principal stress/strain axes rotate during loading. As the transition criterion is fulfilled, the first crack is initiated, as discussed in the previous section. Due to the evolution of the stress and strain state in the medium, a second crack can be localized in another direction.

To account for this situation in a microplane microdamage-to-fracture transition approach, at each time, we identify the microplane system Ω into two non-intersecting subsets Ω^1 and Ω^2, such that Ω^1 contains

---

[6] Notice that similar expression is obtained in [60] using a continuum damage model.

microplanes that are in unloading condition and Ω^2 is a subset that contains microplanes in loading condition (Eq. (10)):

$$\Omega^1 = \{\Omega^\alpha \in \Omega \, : \dot{\omega}^\alpha = 0, \, f^\alpha < 0\} \quad \text{and} \quad \Omega^2 = \{\Omega^\alpha \in \Omega \, : \dot{\omega}^\alpha > 0, \, f^\alpha = 0\} \tag{46}$$

Using the analogy between microplanes and microcracks, one can assume that microplanes belonging to Ω^1 correspond to the family of microcracks that coalesced to form the first crack; in contrast, microplanes belonging to Ω^2 represent still active (opening or dissipating) microcracks. If the transition criterion for the second crack is reached on at least one microplane in Ω^2 then a second crack orthogonal/non-orthogonal to the first one is initiated in the direction of the maximum principal stress at the transition. The available energy for the crack (ϕ_{S_2}) is then obtained through Eq. (44), but the integration for the calculation of the energy dissipation is now performed over Ω^2 only.

Notice that the same transition criterion is adopted for the activation of both the cracks. This is justified because the material is isotropic before the initiation of the microdamage. More studies are needed, however, to better define transition criteria for multiple cracks as well as the more realistic way for calibrating traction-separation laws, in particular for the second crack.

4.2.2. *Algorithm*

Two Boolean variables $flag_1$ and $flag_2$ are used to store the information about the first and second crack respectively. Similar to the single crack case, these variables are initiated with 0 and set to 1 after the respective cracks initiation. Again, the variables related to the discretized displacement jump at both cracks, $\mathbf{e}_1^i$ and $\mathbf{e}_2^i$ respectively, are initiated with $\mathbf{0}$. From now on, down-scripts S_1 and S_2 are used to denote quantities referred to as the first and second crack, respectively.

Here, we assume that the cracks are initiated sequentially, i.e., the second crack is initiated only after the initiation of the first crack. This allows us to obtain $\mathbf{e}_1^i$ in the first step and then the evolution of ω^α due to the rotation of the principal stress/strain axes in the next step. In the below, we focus on the steps involved in the initiation of the second crack:

1. after solving the traction-separation law at the first crack (i.e., computing the enhanced displacement corresponding to the first crack opening), project the updated strain ($\mathbf{Bd} + \mathbf{G}_1\mathbf{e}_1$) on each microplane to calculate ϵ_m^α and ϵ_l^α.
2. recalculate ω^α and $\hat{\phi}_V^\alpha$ using the components of updated strain on each microplane.
3. check the transition criterion on the microplanes belonging to Ω^2, on which microdamage growth takes place after updating the strain and if the transition criterion is fulfilled then the second crack is initiated. Now the coupled traction-continuity conditions are solved. Following the same approach for the case of single crack (see Eq. (45)) and noting that the energy dissipation takes place only on the microplanes belonging to Ω^2, we obtain the energy available for the second crack as:

$$G_{f,S_2} = \hat{\phi}_{S_2} = \frac{1}{\pi}\left(\sum_{\Omega} \left(g_f^\pi - \hat{\phi}_V^\alpha\right) W^\alpha\right) l_c = \hat{\phi}_{S_1} - \frac{1}{\pi}\left(\sum_{\Omega^2} \hat{\phi}_V^\alpha \, W^\alpha\right) l_c \tag{47}$$

5. Representative numerical examples

In this section, the proposed approach presented above is illustrated numerically through some simple examples. First, the characteristic responses of the microplane microdamage model and the strong discontinuity model (after coupling) are studied using a uniaxial tensile loading test in which a single crack is initiated. Second, the effect of continuous/discontinuous transition criteria in the context of the energy regularization technique is studied. Finally, a Willam-like loading numerical experiment is used to illustrate both the initiation and propagation of two non-orthogonal cracks. Notice that, the present work aims to present the proposed formulation and related algorithms. Further work is ongoing to study the structural test cases involving multiple cracks propagating through the specimen.

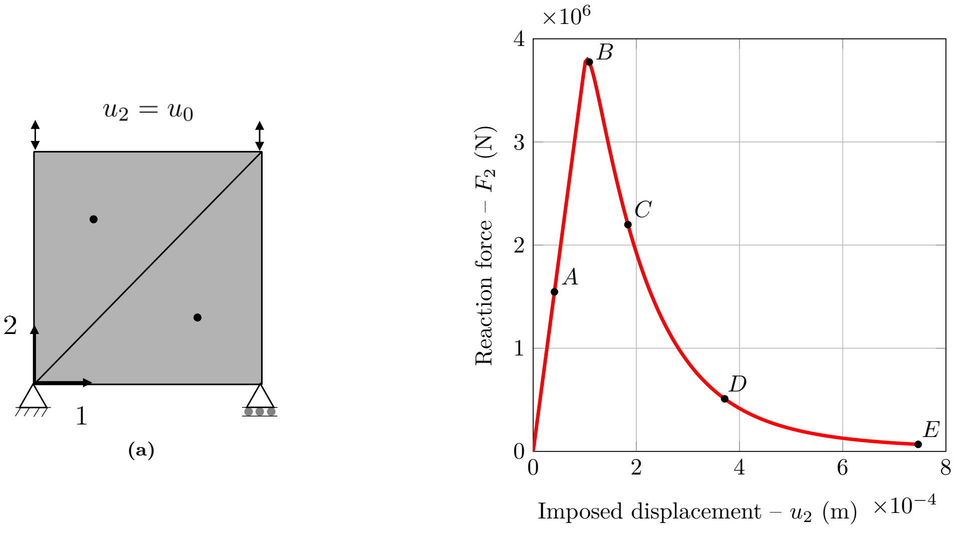

(a)

(b)

Figure 4: FE discretization of the specimen (1 m × 1 m) under vertical loading (a) and the force-displacement curve in vertical direction of microplane microdamage model (b)

5.1. Numerical behavior of microplane microdamage model

Problem setting. We consider a unit quasi-brittle material specimen under plane strain condition, which is discretized using 2 CST elements (Fig. 4a) and apply the loading (vertical imposed displacements) on the upper boundary whereas the bottom boundary is constrained. To illustrate the microplane microdamage model's behavior, we consider the microdamage growth as the only dissipation mechanism (i.e., no cracks are initiated). The material parameters of the microplane microdamage model are Young's modulus, $E = 36$ GPa, Poisson's ratio, $\nu = 0.2$, $\tilde{\epsilon}_0^{\pi} = 10^{-4}$, $\beta = 1$ and $G_f = 1000$ N/m. Here, we chose the value of the parameter β as 1 to completely take into account the contribution of ϵ_l^{α} for $\tilde{\epsilon}^{\alpha}$. Also, $N^{\alpha} = 361$, which gives a microplane for each 0.5° is chosen to ensure high accuracy of the numerical integration. A detailed analysis of the response of the microplane microdamage model for other values of these parameters is shown later. Finally, the reference axis to compute the angle α of the normal $\mathbf{m}^{\alpha}$ of a given microplane is chosen as the axis 1 aligned with the horizontal direction (Fig. 4a).

Global response. The global response of the specimen is shown in Fig. 4b. As expected, the reaction force first increases linearly (elastic phase). Then, a softening phase, corresponding to the progressive evolution of microdamage at microplanes level, is obtained.

Distribution profiles of strain components. The evolution of the distribution profiles of ϵ_m^{α} and ϵ_l^{α} over the microplanes (at Gauss point level) computed at different points along the global curve (Fig. 4b) are given in Figs. 5a and 5b respectively. It can be easily noticed that the distribution of ϵ_m^{α} is symmetric with respect to the direction of loading. Conversely, the distribution of ϵ_l^{α} is anti-symmetric with respect to the direction of loading. The maximum value of ϵ_m^{α} occurs on the microplane corresponding to $\alpha = 90°$ (Fig. 5a), which is aligned with the direction of the loading. For ϵ_l^{α}, the absolute maximum value occurs on the microplanes corresponding to $\alpha = 45°$ and $\alpha = 135°$ (Fig. 5b), whose inclination with the direction of the loading is 45° in clockwise and anti-clockwise sense respectively. It can also be verified numerically that the microplanes whose normal ($\alpha = 0°$ and $\alpha = 180°$ in Fig. 5a) is orthogonal to the direction of loading have negative values of ϵ_m^{α} due to the Poisson's effect.

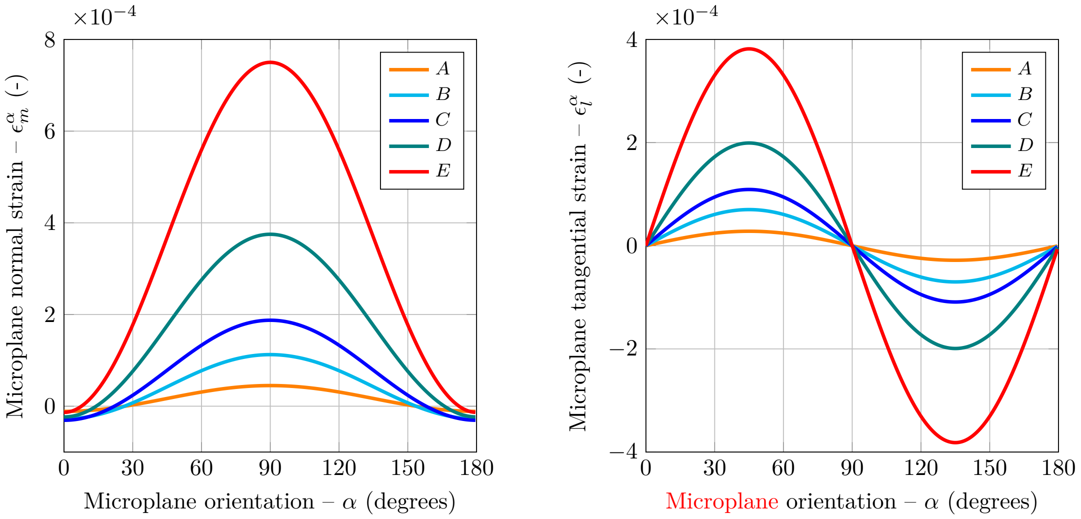

(a) **(b)**

Figure 5: Distribution profiles of ϵ_m^α (a) and ϵ_l^α (b) over the microplane system at various stages of uniaxial loading in vertical direction

Distribution profiles of microdamage and energy dissipation. The evolution of the microdamage distribution profiles over the microplane system is shown in Fig. 6a. Due to induced anisotropy, the evolution of the microdamage is maximum on the microplane whose normal is aligned with the loading direction ($\alpha = 90°$ in Fig. 6a). Owing to the projection of the positive part of the strain tensor, the contribution of the microplanes for negative values of ϵ_m^α is not taken into account for the computation of $\tilde{\epsilon}^\alpha$. Hence, there is no microdamage evolution on the microplanes aligned in the orthogonal direction of the loading ($\alpha = 0°$ and $\alpha = 180°$ in Fig. 6a). The same trend is followed by the energy dissipation profile as shown in Fig. 6b. The maximum energy dissipation occurs on the microplane on which the microdamage is maximum. In the case of microplanes on which there is no evolution of microdamage, the energy dissipation is null.

Influence of the number of microplanes. Here, we point out that it is less time consuming to perform a numerical integration over a 1D domain in the case of the disk microplane system than over a 2D domain in the case of the spherical microplane system. However, for the accuracy of the numerical integration scheme, an optimum number of microplanes must be selected. To achieve that, we study here the influence of N^α on the global response of the uniaxial tensile test. One can observe that at least $N^\alpha = 3$ microplanes are necessary for recovering the elastic properties. Also, convergence in the global curve (Fig. 7a) is achieved for $N^\alpha \geq 21$. In addition to this, relative errors in terms of the force at the peak of the curve (F_{peak}) and the dissipated energy can be defined as, $\Delta F_{peak} = \frac{F_{peak}^{ref} - F_{peak}}{F_{peak}^{ref}}$ and $\Delta\phi_V = \frac{\phi_V^{ref} - \phi_V}{\phi_V^{ref}}$ respectively. Here, the reference values are considered to be the ones corresponding to a large number of microplanes ($N^\alpha = 10000$). The quantities, ΔF_{peak} and $\Delta\phi_V$ are shown in the semi-logarithmic (lin-log) plot (Fig. 7b) from which we can observe that the relative error in terms of both the force at the peak and the energy dissipation is negligible for $N^\alpha \geq 21$ ($10^{1.32}$). As a result of this analysis, we consider $N^\alpha = 21$[7] for the rest of the numerical studies in this work.

---

[7] Note that this result is fully consistent with results presented in the original work on disk microplane model [17], in which the same number of microplanes (21) are considered for numerical integration.

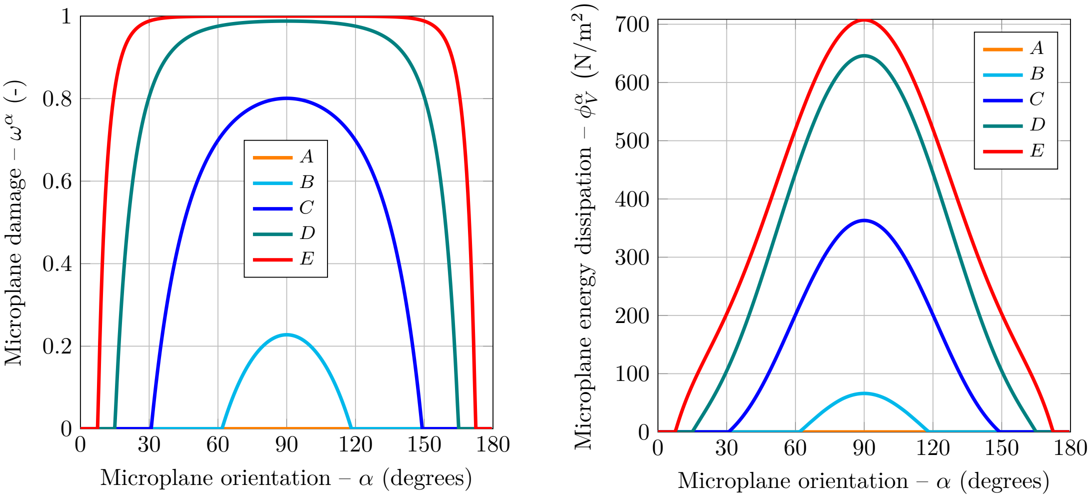

(a) **(b)**

Figure 6: Distribution profiles of ω^α (a) and ϕ_V^α (b) over the microplane system at various stages of uniaxial loading in vertical direction

5.2. Numerical illustration of the transition approach in case of a single crack

Problem setting. The proposed transition approach is illustrated using the same uniaxial tensile loading experiment that is performed in the previous case. In the case of the microplane model, the same material parameters as the ones used in the previous case-study are used; in the case case of the E-FEM, the available fracture energy ($G_{f,S}$) is computed based on the proposed formulation. Besides, to consider a complete interaction between the normal and the tangential components of the displacement jump, we set $\beta_{cr} = 1$. For the sake of illustration, we perform the transition when $\tilde{\epsilon}^\alpha$ on at least one microplane reaches a critical value of $\tilde{\epsilon}^\alpha_{\mathrm{tr}} = 1.5\tilde{\epsilon}^\pi_0 = 1.5 \times 10^{-4}$. However, similar results can be obtained considering different transition criteria and threshold values.

Results. The global force-displacement response in the vertical direction is shown in Fig. 8a. The curve *O*-*A*-*B*-*C* shows the elastic and the damage phases, while the curve *C*-*D* (Figs. 8a and 8b) represents the crack opening phase. Upon unloading at *D*, the crack closes (Figs. 8a and 8b).

Microplane dissipation profiles at the different stages of the test are depicted in Fig. 9. Based on these observations, the evolution of the volumetric and surface energy dissipation during the test can be summarized as follows: (i) the energy dissipation in the bulk takes place during the microdamage growth phase before the transition; (ii) as soon as the crack opening phase begins, there is no more energy dissipation in the bulk and the residual energy (shaded area in Fig. 9) is dissipated at the crack. In this phase, microplanes experience unloading (strain is reduced), the corresponding internal variables no more evolve, and damage is naturally frozen.

In the later example, we will show that when the rotation of principal stress/strain axes happens, the microdamage starts evolving again and energy dissipation takes place in the bulk before initiating a second crack.

Let us note that the smoothness of the global curve Fig. 8a obtained using the transition methodology is an attribute of the exponential softening Eq. (7) and traction-separation laws (Eqs. (40) and (41)) of the microplane microdamage model and the E-FEM, respectively. Note that C^0 continuity is not enforced at the point of transition.

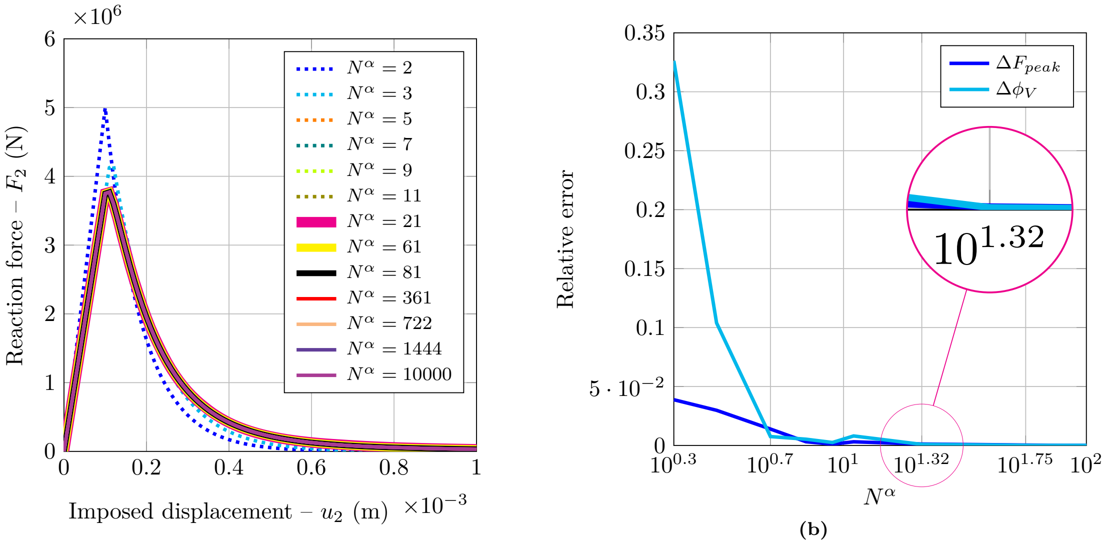

(a)

(b)

Figure 7: Influence of N^α: force-displacement curves in vertical direction (a) and relative error in terms of F_{peak} and ϕ_V (b)

5.3. Mesh dependency studies - effect of different transition criteria

Transition criteria have to be formulated such that the crack initiation, as well as the global (force-displacement) and local (crack opening evolution) responses, are not mesh dependent. In this section, we study the mesh dependency induced by various transition criteria.

Problem setting. A quasi-brittle material bar submitted to a uniaxial loading in the horizontal direction is considered (Fig. 10). We allow the localization band of width w to form only in the central part of the bar by considering the microplane model in this part. In the localization band, we initiate the crack when the transition criterion is fulfilled. The rest of the bar is assumed to behave elastically.

Now, we consider different mesh discretizations of the given specimen using CST elements and parameterizing the width of the weakened element (or elements) in the central portion of the bar. We obtain mesh-1, mesh-2 and mesh-3 by varying $w = 0.2$ m, 0.1 m and 0.05 m while $h = 0.1$ m is kept constant (Fig. 10). The characteristic length (i.e., mesh size) to be used for energetic regularization of the microplane model is chosen as $l_c = w$.

Transition criteria. Here, we consider 2 different formulations for the transition criterion based on: (i) the maximum of the microdamage variables on all microplanes, $\max_\alpha(\omega^\alpha)$; (ii) the maximum energy dissipation on the all microplanes, $\max_\alpha(\phi_V^\alpha)$. The corresponding thresholds at the transition are denoted by, $\omega_{\mathrm{tr}}^\alpha$ and $(\phi_V^\alpha)_{\mathrm{tr}}$ respectively.

Results. Global responses obtained using different transition criteria are given in Figs. 11a and 12a. The corresponding calibrated traction-separation laws are given in Figs. 11b and 12b. For the sake of illustration, we choose the corresponding threshold values at transition of the different parameters as, $\omega_{\mathrm{tr}}^\alpha = 0.75$ and $(\phi_V^\alpha)_{\mathrm{tr}} = 2g_f^\pi/3 \approx 333\ \mathrm{N/m^2}$.

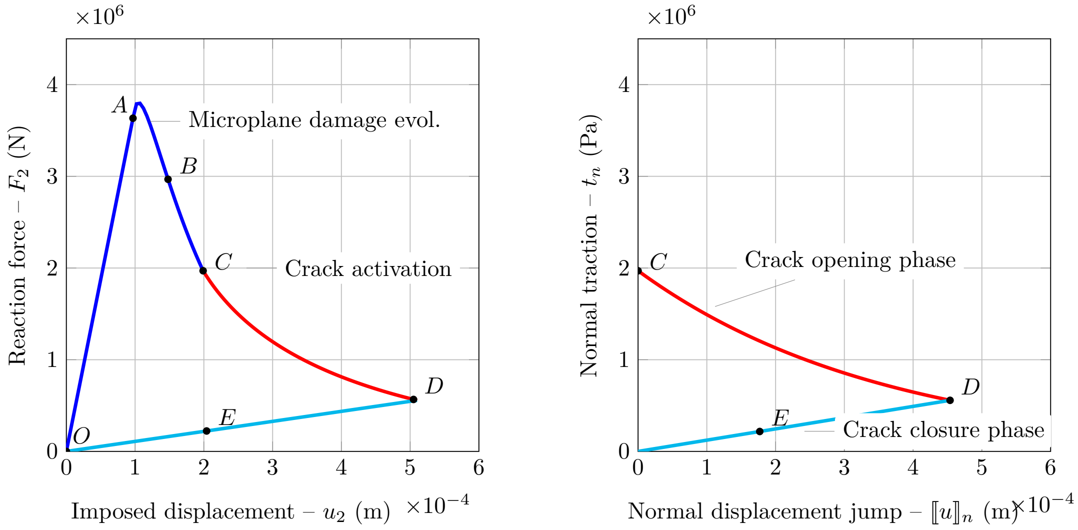

(a) **(b)**

Figure 8: Transition approach for a single crack: global force-displacement curve in vertical direction (a) and traction-separation law after transition (b) for uniaxial loading test

From Fig. 11a, one can observe that when performing the transition based on maximum ω^{α}, the global response is mesh independent before transition due to energetic regularization of the microplane microdamage model, but mesh sensitivity comes into the picture after the opening of the crack. The reason is that the crack is activated at different traction levels (Fig. 11b) for the considered meshes since ω^{α} is not a regularized quantity.

As shown in Figs. 12a and 12b, mesh independent results can be achieved considering a transition based on microplane dissipation. This is explained by the fact that we regularized the energy dissipation of the microplane microdamage model (see Section 2.3). According to these observations, we adopt a transition criterion based on the regularized maximum energy dissipation for the rest of the numerical tests.

5.4. Numerical illustration of the transition approach in the case of non-orthogonal cracks

In this section, we show the capability of the proposed methodology to tackle the localization of non-orthogonal cracks. Let us consider a Willam's test like loading [64]. In this test, the loading is applied in a non-proportional manner in the horizontal and vertical directions that leads to a progressive rotation of principal stress axes. This changes the behavior of the cracks from mode-I to mixed mode. The test is successful if the model is able to handle the mixed mode cracking and dissipate the available energy in multiple directions.

Problem setting. The considered geometry, loading and boundary conditions are given in Fig. 13. Loading is applied (imposed displacements) in two phases. In the first phase, a tensile loading in the vertical direction is applied along with the compression loading in the horizontal direction (to negate the Poisson's effect). After the opening of the first crack, the second phase of the loading starts. In this phase, a combined horizontal tensile loading and shear loading along with the vertical tensile loading is applied in a non-proportional manner.

The considered material parameters are Young's modulus = 10 GPa, Poisson's ratio, = 0.20, $\tilde{\epsilon}^{\alpha} = 10^{-4}$, $\beta = 1$, $N^{\alpha} = 21$, $G_f = 500$ N/m and $\beta_{cr} = 1$. In order to illustrate the role of the chosen transition

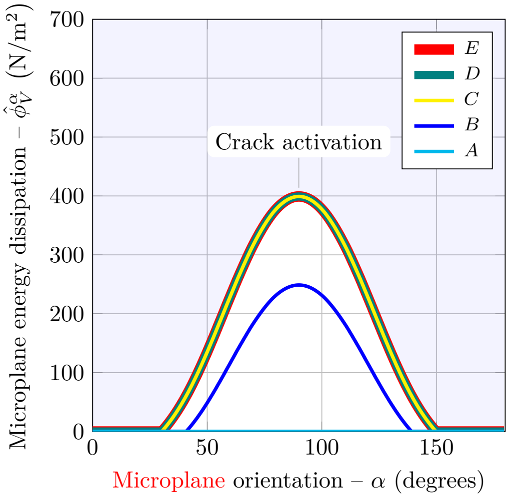

Figure 9: Distribution profiles of $\hat{\phi}_V^\alpha$ over the microplane system at various stages of uniaxial loading test using transition approach

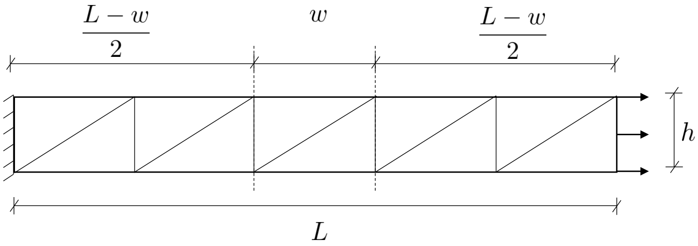

Figure 10: Specimen for mesh dependency study: a quasi-brittle bar under tensile loading

threshold on obtained results (and in particular on the deviation angle between the two cracks), we first perform the transition at a small energy dissipation level ($(\phi_V^\alpha)_{\mathrm{tr}} = 20\%$ of g_f^π). Later, higher transition energy thresholds are considered.

Results. The main results can be summarized as follows:

(i) In the first phase of the loading, a single crack is initiated. In Fig. 14a, the evolution of different components of stress is shown. Here, the microdamage evolution starts at A and the crack opening starts at B (transition point). From the microdamage profiles in Fig. 15a, we can observe that the microplanes close to the orthogonal direction of the loading ($\alpha = 0°$) are still in the elastic regime. As expected, all the microplanes unload after the crack opening and there is no more energy dissipation on the microplanes (Fig. 15b). During this phase, the crack behaves in mode-I and only the normal displacement of the first crack ($[\![u]\!]_{n_1}$) evolves (Fig. 14b).

(ii) In the second phase, a combined vertical, shear and horizontal loading is applied leading to the continuous rotation of principal strain axes. Consequently, the microdamage evolution first takes place on the microplanes which remained elastic during the first phase of loading and then on the microplanes that entered the unloading regime after the first crack is opened (Fig. 15a). The corresponding energy dissipation profiles are shown in Fig. 15b.

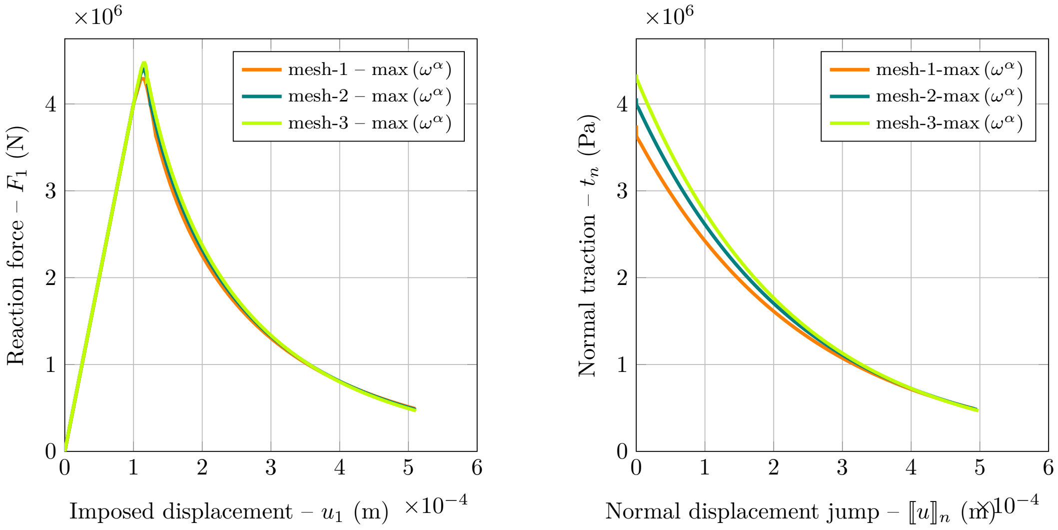

(a) **(b)**

Figure 11: Mesh objectivity of the transition criterion based on max $(\tilde{\varepsilon}^\alpha)$ and max (ω^α): comparisons of force-displacement curves in horizontal direction (a) and local traction-separation laws (b) for different meshes by considering $l_c = w$

The second crack is initiated when the transition criterion is fulfilled on at least one of the microplanes on which the microdamage growth takes place during the second phase of loading (Ω^2). This crack is opened at 78.81° to the first crack. The energy dissipation profiles at the opening of the second crack are shown in Fig. 15b.

During the second phase, the first crack begins to slide due to the rotation of the principal stress axes as soon as the non-proportional loading is applied. This leads to the evolution of ($[\![u]\!]_{s_1}$) from B in Fig. 14b. Furthermore, the constant rotation of the principal stress axes compel the cracks to behave in mixed mode condition to satisfy the local equilibrium. This leads to the evolution of both $[\![u]\!]_{n_2}$ and $[\![u]\!]_{s_2}$ from the onset of second crack at C. Moreover, the angle between the two non-orthogonal cracks also depends on the level of energy dissipation at which the transition is performed.

Influence of the threshold of transition criterion. To show the role of transition criterion threshold in the obtained response, we repeat the same test for different levels of energy dissipation at transition. For the sake of illustration, we now perform the transition after the dissipation reaches 40% and 60% of g_f^π on at least one microplane.

It is observed from the evolution of the components of stress tensor (Figs. 14a, 16a and 16b) that the peaks of the stress components, σ_{11} and σ_{12} are reduced as the threshold of the transition criterion increases. This is explained using the corresponding microdamage and energy dissipation profiles (Figs. 17a and 17b) before the activation of the first and second cracks (B and C in Figs. 16a and 16b) respectively. It can be concluded from Figs. 17a and 17b that, as the threshold of transition criterion increases, higher is the level of microdamage before the activation of the second crack and also lower is the available energy. Moreover, as the level of energy dissipation at transition increases, the second crack is rotated further from the first crack. It is observed that the angle between the two cracks is 81° and 97° in the cases for which the level of energy dissipation at transition is 40% and 60% of g_f^π respectively. In other words, higher the threshold level, higher the tendency to the localization of a second crack that is orthogonal to the first one.

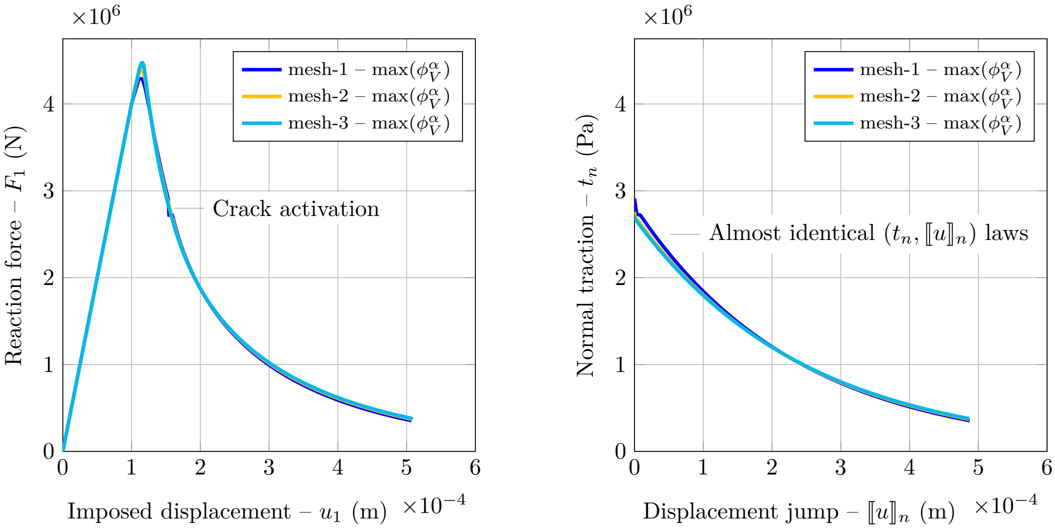

(a) **(b)**

Figure 12: Mesh objectivity of the transition criterion based on max(ϕ_V^α): comparisons of force-displacement curves in horizontal direction (a) and local traction-separation laws (b) for different meshes by considering $l_c = w$

Characterization of anisotropy. Before the initiation of the crack, the principal stress and strain axes stay parallel with each other as we assumed an isotropic elastic response prior to the microdamage growth. However, due to induced anisotropy, the principal stress and strain axes rotates at different rate with respect to a fixed direction. Using Willam's test, rate of anisotropy can be quantified by computing the difference between the asymptotic values of the rotation of the principal stress and strain axes during the loading history.

Let γ_σ and γ_ϵ be the rotation of the maximum principal stress and strain axes respectively with respect to the vertical direction. Here, we consider two cases; the first one is the case in which we allow only one crack to initiate, whereas in the second case (which is the present case) two non-orthogonal cracks are initiated. The evolution of γ_ϵ remains the same in both cases as it is related to the applied loading while the evolution of γ_σ is compared for both the cases in Fig. 18. As shown in this figure γ_σ becomes non-zero at the beginning of the second phase and, if the second crack is not initiated, then it keeps on increasing before reaching an asymptotic value of 90°, i.e., the maximum principal direction is aligned with the horizontal direction. However, as the second crack localizes, reduction takes place for all the stress components. Hence, its asymptotic value (γ_σ^{asy}) is different from the one crack case which is obtained as, $\gamma_\sigma^{\text{asy}} = 83.5°$, $81.51°$ and $79.7°$ for the threshold at 20%, 40% and 60% of g_f^π respectively. The asymptotic value of the rotation of the maximum principal strain axis ($\gamma_\epsilon^{\text{asy}}$) is obtained as $41.67°$. Finally, the rate of anisotropy [65] is computed according to, $(\gamma_\sigma^{\text{asy}} - \gamma_\epsilon^{\text{asy}})/\gamma_\epsilon^{\text{asy}} \times 100$, which gives 50%, 48.8% and 47.7% for the threshold at 20%, 40% and 60% of g_f^π respectively. These results can be compared to the ones obtained using an enhanced anisotropic damage model [66] which is 46%.

6. Conclusions

In this paper, we exposed a novel approach for modeling strain localization process by coupling the microplane and strong discontinuity models. In this manner, the anisotropic nature of the damage growth is

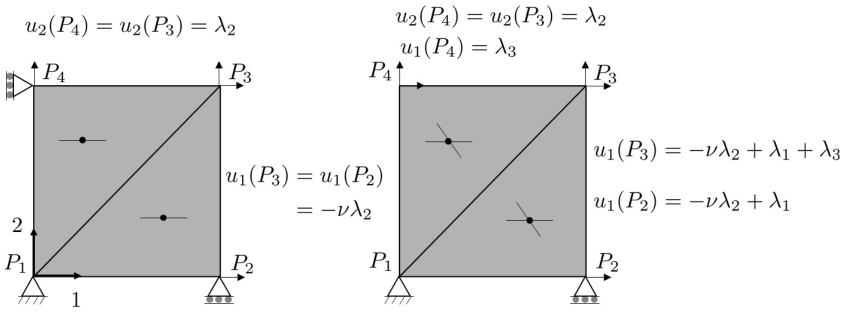

Figure 13: FE discretization of the specimen (1 m × 1 m) and the expected crack orientations under Willam's like loading

taken into account before the formation of cracks. Also, a framework for modeling multiple localized cracks is presented.

In the microplane model, a computationally effective disk microplane system is used under the plane strain assumption instead of a spherical one. Simple constitutive laws using a single microdamage variable are assumed and the quantities at a unit volume, especially stress tensor and energy dissipation, are obtained from microplanes.

Two intersecting strong discontinuities are modeled in the extended E-FEM in which coupled traction continuity conditions are formulated by assuming that two crack surfaces are superposed. In this way, the local equilibrium at both the crack surfaces is satisfied. The discrete constitutive law that takes into account the mixed-mode cracking is considered. However, we tackle here only the case of the formation of two cracks. Such consideration is subjected to the experimental/industrial case, which is addressed by the proposed formulation. Some guidelines have to be developed for limiting the number of cracks to be considered in this framework.

After coupling both the proposed models in a damage-to-fracture transition framework, the energy available for the crack is calculated by taking into account the energy dissipated in the localization band. This is achieved by computing (at the transition instant) the residual energy available at the microplanes level, which is then dissipated at the crack surface.

The main interest of using the microplane microdamage model for modeling the response of the bulk material is that damage-to-fracture transition criteria can be written in terms of the quantities that are available on each microplane, thus taking into account the induced anisotropy. In this work, the selected transition criterion for the multiple cracks initiation is based on the maximum energy dissipation on the microplane system. This proves to be an efficient one since it keeps mesh objectivity of the results.

As a first step toward the description of multicracking within the framework of E-FEM, including damage-to-cracking transition, the proposed model has limitations that have been identified. First, crack branching is not explicitly taken into account. However, given the model's formulation, implementing it seems possible based upon related works in the literature [67, 68, 69]. Second, a limited number of local dissipative mechanisms are considered. Adding refined mechanisms, such as frictional sliding occurring between the crack surfaces, seems straightforward given the vectorial nature of the constitutive laws considered in this job. Last, the computational cost of the proposed model is significant due to the microplane framework. However, dedicated work could be done to reduce it by considering the numerical construction of off-line vademecum according to the proposal made by [70].

Finally, transition criteria could be improved by numerical experimentation techniques such as the virtual testing tools [71] based on the discrete element method. The key question to address is, can an objective

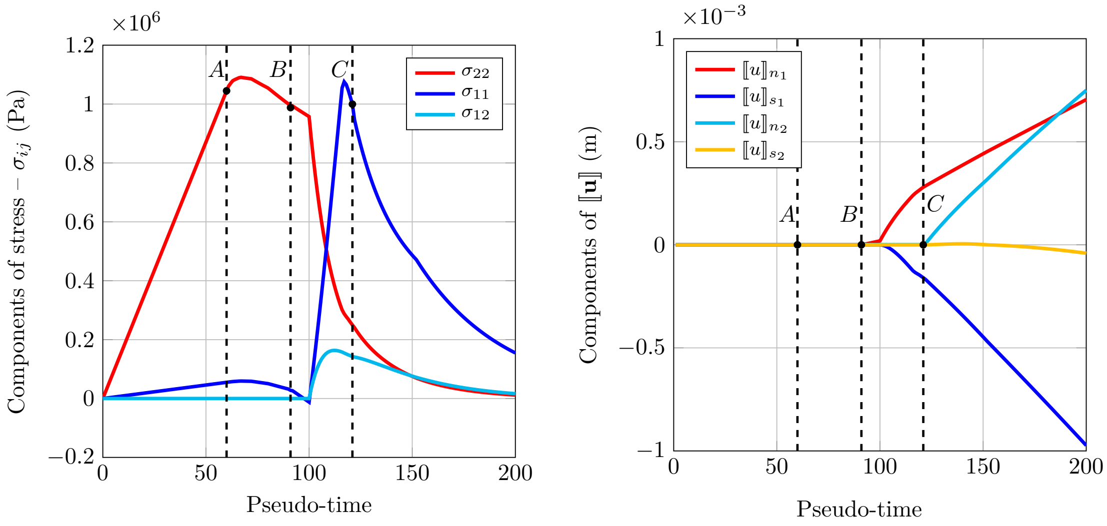

(a) **(b)**

Figure 14: Time evolution of the components of stress (a) and displacement jump (b) - Willam's like loading test using transition approach for the threshold at 20% g_f^π

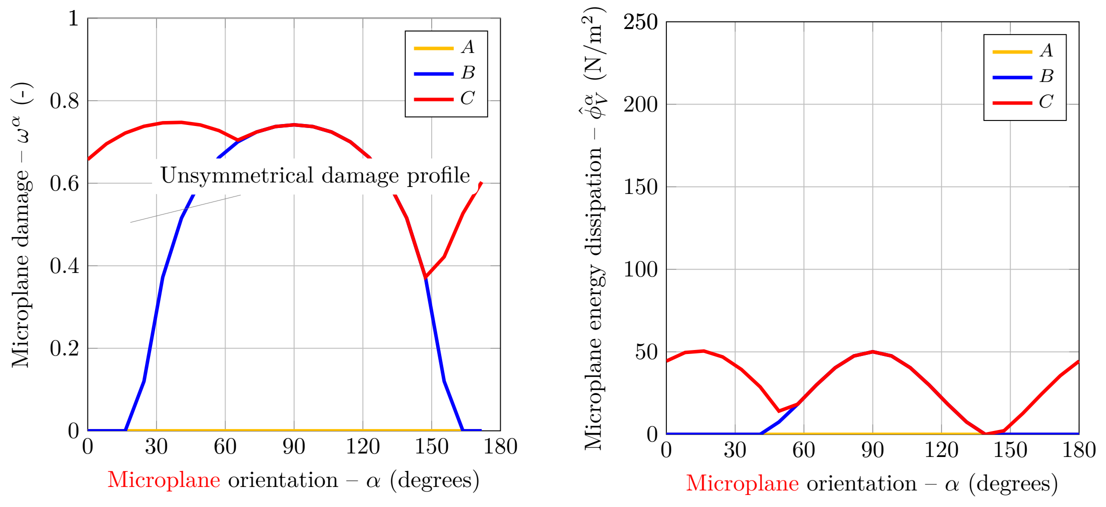

(a) **(b)**

Figure 15: Distribution profiles of ω^α (a) and $\hat{\phi}_V^\alpha$ (b) over the microplane system at various stages of Willam's like loading test using transition approach for the threshold at 20% of g_f^π

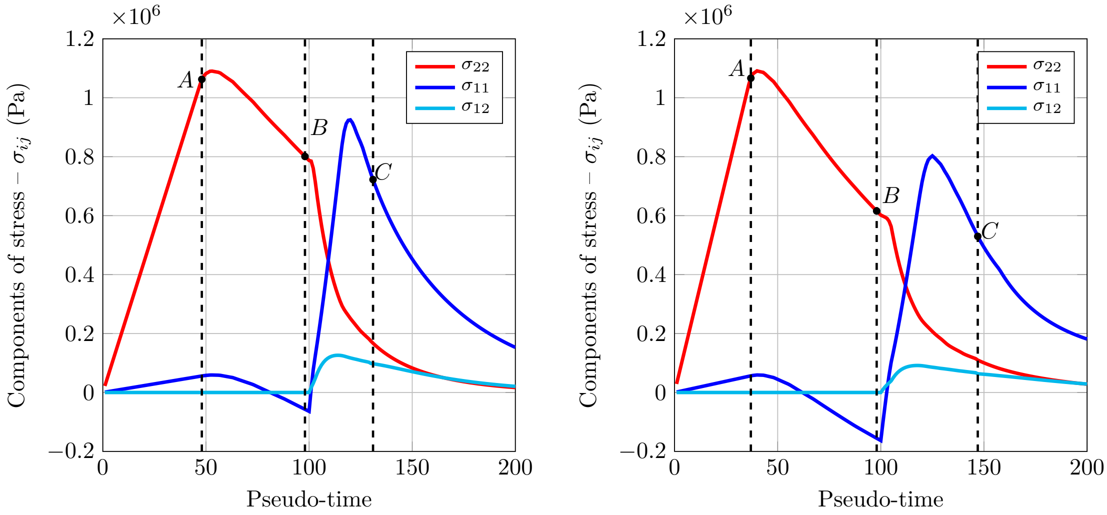

(a) **(b)**

Figure 16: Time evolution of the components of stress - Willam's like loading test using transition approach for the threshold at 40% of g_f^π (a), 60% of g_f^π (b)

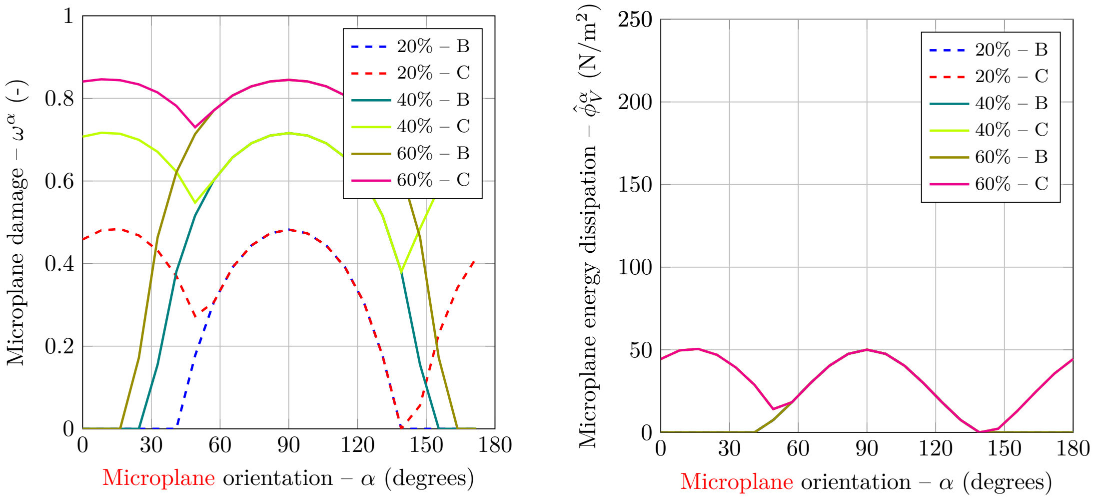

(a) **(b)**

Figure 17: Comparison of distribution profiles of ω^α (a) and $\hat{\phi}_V^\alpha$ (b) over the microplane system at various stages of Willam's like loading test using transition approach for different thresholds of transition criterion

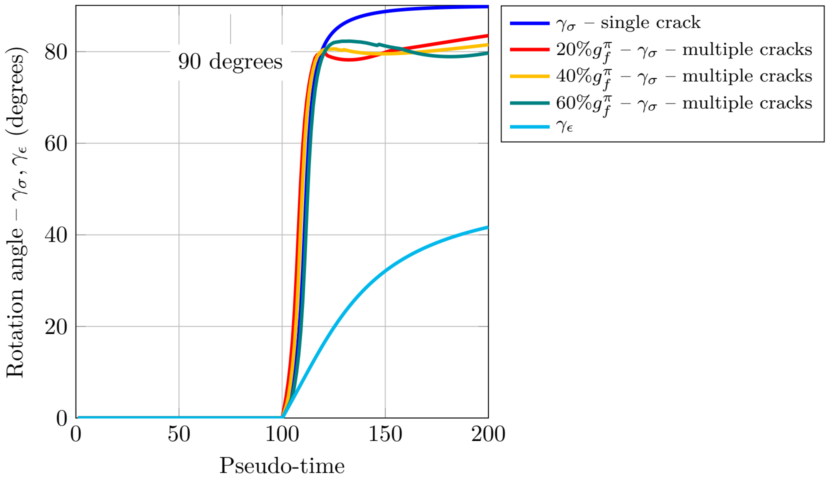

Figure 18: Time evolution of the rotation of the maximum principal stress and strain axes with respect to the vertical direction - Willam's like loading test using proposed transition approach and augmented E-FEM

transition criterion be formulated? Also, another important point to clarify is how to separate the energy dissipation between initiated cracks? In this case, the possibility of the localization of the second crack is to be investigated. In the proposed transition formulation, we initiate both the cracks in the direction of the principal stress. These aspects, particularly the crack initiation direction and the orientation between the cracks, also need to be studied in detail.

Acknowledgments

The authors declare that they have no known competing financial interests or personal relationships that could have appeared to influence the work reported in this paper. S. Kakarla and G. Rastiello were supported by the SEISM Institute (`http://www.institut-seism.fr`).

Appendix A. Regularized damage evolution model

Given the exponential damage evolution law Eq. (7), the energetic regularization problem comes into finding the scalar parameter $B = B(l_c)$ such that:

$$\frac{G_f}{2l_c} = \int_0^{t_0} \left(E_m \epsilon_m^\alpha \dot{\epsilon}_m^\alpha + E_l \epsilon_l^\alpha \dot{\epsilon}_l^\alpha \right) \, dt + \int_{t_0}^{\infty} \frac{\tilde{\epsilon}_0^\pi}{\kappa^\alpha} \exp^{\left(-B(\kappa^\alpha - \tilde{\epsilon}_0^\pi)\right)} \left(E_m \epsilon_m^\alpha \dot{\epsilon}_m^\alpha + E_l \epsilon_l^\alpha \dot{\epsilon}_l^\alpha \right) \, dt \tag{A.1}$$

where t_0 is the time instant at which the microplane equivalent strain reaches the strain level corresponding to damage activation.

This requires analytically integrating previous equation, which is possible only for the hypothetical case of $\nu = 0$ (i.e., $E_m = E_l = E$) and $\beta = 1$. Consider a uniaxial tensile loading in the direction of axis 2 (or equivalently 1), i.e., $\boldsymbol{\epsilon} = \epsilon_{22} \, \mathbf{x}_2 \otimes \mathbf{x}_2$. Since in this case $\epsilon_m^{\alpha +} = \epsilon_m = \sin^2 \alpha \, \epsilon_{22}$ and $\epsilon_l^{\alpha +} = \epsilon_l = \sin \alpha \cos \alpha \, \epsilon_{22}$, the first term of the previous equation reads:

$$E \int_0^{t_0} \left(\epsilon_m^\alpha \dot{\epsilon}_m^\alpha + \epsilon_l^\alpha \dot{\epsilon}_t^\alpha \right) dt = E \sin^2 \alpha \int_0^{t_0} \epsilon_{22} \, d\epsilon_{22} = E \int_0^{\tilde{\epsilon}_0^\pi} \tilde{\epsilon}^\alpha \, d\tilde{\epsilon}^\alpha = \frac{1}{2} E \left(\tilde{\epsilon}^\alpha \right)^2 \tag{A.2}$$

where, we used the relationship $\tilde{\epsilon}^\alpha = \epsilon_{22} \sin\alpha$. Furthermore, during the damage phase, the history variable and its rate of variation reads:

$$\kappa^\alpha = \tilde{\epsilon}^\alpha \quad \text{and} \quad \dot{\kappa}^\alpha = \frac{\epsilon_m^\alpha \dot{\epsilon}_m^\alpha + \epsilon_l^\alpha \dot{\epsilon}_l^\alpha}{\tilde{\epsilon}^\alpha}. \tag{A.3}$$

So, we can rewrite the second contribution figuring in Eq. (A.1) in terms of the sole variable κ^α. As a consequence, Eq. (A.1) can be rewritten as:

$$\frac{G_f - E\left(\tilde{\epsilon}^\alpha\right)^2 l_c}{2 l_c} = E\tilde{\epsilon}_0^\pi \int_{\tilde{\epsilon}_0^\pi}^{\infty} \exp^{\left(-B\left(\kappa^\alpha - \tilde{\epsilon}_0^\pi\right)\right)} \, d\kappa^\alpha \tag{A.4}$$

for each microplane, except the microplane whose normal is orthogonal to the loading direction. Finally, after performing the analytical integration, the material parameter B is obtained in terms of l_c as:

$$B = \frac{2E\tilde{\epsilon}_0^\pi l_c}{G_f - E\left(\tilde{\epsilon}_0^\pi\right)^2 l_c} \tag{A.5}$$

Appendix B. Elastic coefficients of the microplane microdamage model

Let us consider the stress tensor obtained from the components on each microplane and focus on the elastic response only:

$$\boldsymbol{\sigma} = \frac{1}{\pi} \int_\Omega \left(E_m \epsilon_m^\alpha \mathbf{M}^\alpha + E_l \epsilon_l^\alpha \mathbf{L}^\alpha\right) \, dS \tag{B.1}$$

Now substituting the expressions for ϵ_m^α and ϵ_l^α, Eq. (1) in Eq. (B.1), we obtain the stress tensor in component form as:

$$\begin{aligned} \sigma_{ij} = \frac{1}{\pi} \int_\Omega & \left[E_m(\cos^2\alpha\epsilon_{11} + \sin^2\alpha\epsilon_{22} + 2\sin\alpha\cos\alpha\epsilon_{12})M_{ij}^\alpha\right] \, dS + \\ & \frac{1}{\pi} \int_\Omega \left[E_l(-\sin\alpha\cos\alpha\epsilon_{11} + \sin\alpha\cos\alpha\epsilon_{22} + (\cos^2\alpha - \sin^2\alpha)\epsilon_{12})L_{ij}^\alpha\right] \, dS \end{aligned} \tag{B.2}$$

Finally, the microplane constants can be computed by imposing the equality on the stiffness matrices of the elastic constitutive model obtained from microplane model after performing analytical integration of Eq. (B.2) and the Hooke's law under plane strain conditions which is written using Lame's constants (λ, μ) as:

$$\begin{Bmatrix} \sigma_{11} \\ \sigma_{22} \\ \sigma_{21} \end{Bmatrix} = \frac{1}{4} \begin{bmatrix} 3E_m + E_l & E_m - E_l & 0 \\ E_m - E_l & 3E_m + E_l & 0 \\ 0 & 0 & 2(E_m + E_l) \end{bmatrix} \begin{Bmatrix} \epsilon_{11} \\ \epsilon_{22} \\ \epsilon_{21} \end{Bmatrix} = \begin{bmatrix} \lambda + 2\mu & \lambda & 0 \\ \lambda & \lambda + 2\mu & 0 \\ 0 & 0 & 2\mu \end{bmatrix} \begin{Bmatrix} \epsilon_{11} \\ \epsilon_{22} \\ \epsilon_{21} \end{Bmatrix} \tag{B.3}$$

and from this we obtain:

$$E_m = 4\lambda + 2\mu - 2\lambda = 2(\lambda + \mu), \qquad E_l = 2\left(\mu - \lambda\right) \tag{B.4}$$

Bibliography

[1] A. HUESPE, J. OLIVER, Crack models with embedded discontinuities, in: Numerical Modeling of Concrete Cracking, Springer, 2011, pp. 99–159.

[2] K. WILLAM, E. WARNKE, Constitutive model for the triaxial behaviour of concrete, IABSE Seminar on Concrete Structures Subjected to Triaxial Stress, Bergamo, Italy (1975) 1–31.

[3] N. OTTOSEN, A. SCORDELIS, A failure criterion for concrete, Journal of Engineering Mechanics 103(4) (1977) 527–535.

[4] R. de BORST, Smeared crack analysis of reinforced concrete beams and slabs failing in shear, in: Proc. Int. Conf. on Computer Aided Analysis and Design of Concrete Struc., Prineridge Press, 1985, pp. 261–273.

[5] J. G. ROTS, Smeared and discrete representations of localized fracture, Current Trends in Concrete Fracture Research, Springer 46 (1991) 45–59.

[6] R. de BORST, P. NAUTA, Non-orthogonal cracks in smeared finite element model, Engineering Computations 124(8) (1998) 842–851.

[7] J. MAZARS, Application de la mécanique de l'endommagement au comportement non liéaire et à la rupture du béton de structure, Thèse de doctorat, Université Pierre et Marie Curie (1984).

[8] J. LEMAITRE, J. MAZARS, Damage mechanics applied to nonlinear behaviour up to failure of concrete structures (1982).

[9] J. LEMAITRE, J. CHABOCHE, Mechanics of Solid Materials, Cambridge University Press, 1990.

[10] J. CHABOCHE, Damage induced anisotropy: on the difficulties associated with the active/passive unilateral condition, International Journal of Damage Mechanics 1(2) (1992) 148–171.

[11] Z. BAŽANT, B. OH, Microplane model for progressive fracture of concrete, Journal of Engineering Mechanics 111(4) (1985) 559–582.

[12] Z. BAŽANT, Microplane model for strain-controlled inelastic behaviour, Mechanics of Engineering Materials 114(10) (1984) 45–59.

[13] I. CAROL, Z. BAŽANT, Damage and plasticity in microplane theory, International Journal for Solids and Structures 34 (1997) 3807–3835.

[14] E. KUHL, P. STEINMANN, I. CAROL, A thermodynamically consistent approach to microplane theory. part ii. dissipation and inelastic constitutive modeling, International journal of solids and structures 38 (17) (2001) 2933–2952.

[15] Z. BAŽANT, P. PRAT, Microplane model for brittle-plastic material:i. theory, Journal of Engineering Mechanics 114(10) (1988) 1672–1687.

[16] Z. BAŽANT, Microplane model for concrete. i: Stress-strain boundaries and finte strain, Journal of Engineering Mechanics 122(3) (1996) 245–254.

[17] H. PARK, H. KIM, Microplane model for reinforced-concrete planar members in tension-compression, Journal of Structural Engineering 129 (3) (2003) 337–345.

[18] M. MATALLAH, C. LA BORDERIE, O. MAUREL, A practical method to estimate crack openings in concrete structures, International Journal for Numerical and Analytical Methods in Geomechanics 34 (15) (2010) 1615–1633.

[19] C. OLIVER-LEBLOND, D. ARNAUD, , F. RAGUENEAU, B. RICHARD, Non-intrusive global/local analysis for the study of fine cracking, International Journal for Numerical and Analytical Methods in Geomechanics 37 (8) (2013) 973–992.

[20] J. OLIVER, Modeling strong discontinuities in solid mechanics via strain softening constitutive equations. part 1: Fundamentals, International Journal for Numerical Methods in Engineering 39(21) (1996) 3575–3600.

[21] J. OLIVER, Modeling strong discontinuities in solid mechanics via strain softening constitutive equations. part 2: Numerical simulation, International Journal for Numerical Methods in Engineering 39(21) (1996) 3601–3623.

[22] M. ORTIZ, L. YVES, A. NEEDLEMAN, A finite element method for localized failure analysis, Computer Methods in Applied Mechanics and Engineering 61(03) (1987) 189–214.

[23] T. BELYTSCHKO, T. BLACK, Elastic crack growth in finite elements with minimal remeshing, International Journal for Numerical Methods in Engineering 45(5) (1999) 601–620.

[24] N. MOES, J. DOLBOW, T. BELYTSCHKO, A finite element method for crack growth without remeshing, International Journal for Numerical Methods in Engineering 46 (1999) 131–150.

[25] J. SIMO, J. OLIVER, F. ARMERO, An analysis of strong discontinuities induced by strain softening in rate-independent inelastic solids, Computational Mechanics 12(09) (1993) 277–296.

[26] J. OLIVER, M. CERVERA, O. MANZOLI, Strong discontinuities and continuum plasticity models: The strong discontinuity approach, International Journal of Plasticity 15 (1999) 319–351.

[27] N. SUKUMAR, D. L. CHOPP, N. MOES, T. BELYTSCHKO, Modeling holes and inclusions by level sets in the extended finite-element method, Computer methods in applied mechanics and engineering 190(46) (2001) 6183–6200.

[28] E. SCHLANGEN, E. J. GARBOCZI, Fracture simulations of concrete using lattice models: computational aspects, Engineering fracture mechanics 57 (2-3) (1997) 319–332.

[29] A. SATTARI, Z. RIZVI, H. MOTRA, F. WUTTKE, Meso-scale modeling of heat transport in a heterogeneous cemented geomaterial by lattice element method, Granular Matter 19 (4) (2017) 66.

[30] M. NIKOLIĆ, A. IBRAHIMBEGOVIC, Rock mechanics model capable of representing initial heterogeneities and full set of 3d failure mechanisms, Computer Methods in Applied Mechanics and Engineering 290 (2015) 209–227.

[31] M. NIKOLIĆ, E. KARAVELIĆ, A. IBRAHIMBEGOVIC, P. MIŠČEVIĆ, Lattice element models and their peculiarities, Archives of Computational Methods in Engineering 25 (3) (2018) 753–784.

[32] J. MAZARS, G. PIJAUDIER-CABOT, From damage to fracture mechanics and conversely: a combined approach, International journal of solids and structures 33 (20-22) (1996) 3327–3342.

[33] A. SIMONE, G. WELLS, L. SLUYS, From continuous to discontinuous failure in a gradient-enhanced continuum damage model, Computer Methods in Applied Mechanics and Engineering 192 (41-42) (2003) 4581–4607.

[34] C. COMI, S. MARIANI, U. PEREGO, An extended fe strategy for transition from continuum damage to mode i cohesive crack propagation, International Journal for Numerical and Analytical Methods in Geomechanics 31 (2) (2007) 213–238.

[35] F. CAZES, M. CORET, A. COMBESCURE, A. GRAVOUIL, A thermodynamic method for the construction of a cohesive law from a nonlocal damage model, International Journal of Solids and Structures 46 (6) (2009) 1476–1490.

[36] F. ARMERO, K. GARIKIPATI, Recent advances in the analysis and numerical simulation of strain localization in inelastic solids, in: O. Owen, E. Hinton (Eds.), Proceedings of Computational Plasticity IV, Barcelona. CIMNE, 1995, pp. 547–561.

[37] J. OLIVER, On the discrete constitutive models induced by strong discontinuity kinematics and continuum constitutive equations, International Journal of Solids and Structures 37 (2000) 7207–7229.

[38] B. Richard, E. Kishta, C. Giry, F. Ragueneau, Strong discontinuity analysis of a class of anisotropic continuum damage constitutive models–part i: Theoretical considerations, Mechanics Research Communications 86 (2017) 32–36.

[39] E. KUHL, E. RAMM, Microplane modelling of cohesive frictional materials, European Journal of Mechanics - A/Solids 19 (2000) S121–S144.

[40] S. FICHANT, Endommagement et anisotropie induite du béton de structures: modélisations approchées, Ph.D. thesis, Cachan, Ecole normale supérieure (1996).

[41] I. CAROL, M. JIRÁSEK, Z. BAŽANT, A thermodynamically consistent approach to microplane theory. part i. free energy and consistent microplane stresses, International Journal of Solids and Structures 38 (17) (2001) 2921–2931.

[42] E. KUHL, E. RAMM, On the linearization of the microplane model, Mechanics of Cohesive-frictional Materials: An International Journal on Experiments, Modelling and Computation of Materials and Structures 3 (4) (1998) 343–364.

[43] Z. BAŽANT, B. OH, Crack band theory for fracture of concrete, Matériaux et construction 16 (3) (1983) 155–177.

[44] J. ČERVENKA, Z. BAŽANT, M. WIERER, Equivalent localization element for crack band approach to mesh-sensitivity in microplane model, International Journal for Numerical Methods in Engineering 62 (5) (2005) 700–726.

[45] Z. BAŽANT, G. di LUZIO, Nonlocal microplane model with strain–softening yield limits, International Journal of Solids and Structures 41 (24-25) (2004) 7209–7240.

[46] I. ZREID, M. KALISKE, A gradient enhanced plasticity–damage microplane model for concrete, Computational Mechanics 62 (5) (2018) 1239–1257.

[47] M. JIRÁSEK, M. BAUER, Numerical aspects of the crack band approach, Computers & structures 110 (2012) 60–78.

[48] D. XENOS, P. GRASSL, Comparison of nonlocal and crack-band damage-plasticity approaches for modelling the failure of reinforced concrete structures, in: N. Bićanić, M. H., M. G., R. de BORST (Eds.), Computational modelling of concrete structures, 2014.

[49] S. PIETRUSZCZAK, Z. MROZ, Finite element analysis of deformation of strain-softening materials, International Journal for Numerical Methods in Engineering 17 (3) (1981) 327–334.

[50] J. OLIVER, A consistent characteristic length for smeared cracking models, International Journal for Numerical Methods in Engineering 28 (2) (1989) 461–474.

[51] O. MANZOLI, P. SHING, Stress hybrid finite elements with multiple embedded cracks, Proceedings of FraMCoS-5 (2004) 123–130.

[52] G. WELLS, L. SLUYS, Three-dimensional embedded discontinuity model for brittle fracture, International Journal of Solids and Structures 38 (5) (2001) 897–913.

[53] D. BRANCHERIE, Modèles continus et discrets pour les problèmes de localisation et de rupture fragile et/ou ductile, Thèse de doctorat, Ecole Normale Supérieure de Cachan. (2003).

[54] K. WASHIZU, On the variational principles of elasticity and plasticity, Technical Report 25-18, Aeroelastic and Structures Research Laboratory, MIT Press, Cambridge 46 (1955) 131–150.

[55] M. JIRÁSEK, Comparative study on finite elements with embedded discontinuities, Computer Methods Applied Mechanics and Engineering 188 (2000) 307–330.

[56] F. CAZES, G. MESCHKE, M. M. ZHOU, Strong discontinuity approaches: An algorithm for robust performance and comparative assessment of accuracy, International Journal of Solids and Structures 96 (2016) 355–379.

[57] P. PEGON, A. ANTHOINE, Numerical strategies for solving continuum damage problems with softening: application to the homogenization of masonry, Computers & structures 64 (1-4) (1997) 623–642.

[58] B. RICHARD, G. RASTIELLO, C. GIRY, F. RICCARDI, R. PAREDES, E. ZAFATI, S. KAKARLA, C. LEJOUAD, Castlab: an object-oriented finite element toolbox within the matlab environment for educational and research purposes in computational solid mechanics, Advances in Engineering Software 128 (2019) 136–151.

[59] J. ALFAIATE, G. WELLS, L. SLUYS, On the use of embedded discontinuity elements with crack path continuity for mode-i and mixed-mode fracture, International Journal for Solids and Structures 38 (2001) 2933–2952.

[60] Y. WANG, H. WAISMAN, From diffuse damage to sharp cohesive cracks: A coupled xfem framework for failure analysis of quasi-brittle materials, Computer Methods in Applied Mechanics and Engineering 299 (2016) 57–89.

[61] S. CUVILLIEZ, F. FEYEL, E. LORENTZ, S. MICHEL-PONNELLE, A finite element approach coupling a continuous gradient damage model and a cohesive zone model within the framework of quasi-brittle failure, Computer methods in applied mechanics and engineering 237 (2012) 244–259.

[62] T. SAKSALA, D. BRANCHERIE, I. HARARI, A. IBRAHIMBEGOVIC, Combined continuum damage-embedded discontinuity model for explicit dynamic fracture analyses of quasi-brittle materials, International Journal for Numerical Methods in Engineering 101 (3) (2015) 230–250.

[63] C. COMI, S. MARIANI, U. PEREGO, From localized damage to discrete cohesive crack propagation in nonlocal continua, in: Proceedings of the Fifth World Congress on Computational Mechanics (WCCM V), Vienna University of Technology, 2002.

[64] K. WILLAM, E. PRAMONO, S. STURE, Fundamental issues of smeared crack models, in: Fracture of concrete and rock, Springer, 1989, pp. 142–157.

[65] I. BITAR, B. RICHARD, Mindlin-reissner plate formulation with enhanced kinematics: Theoretical framework and numerical applications, Engineering Fracture Mechanics (2020) 106839.

[66] E. KISHTA, B. RICHARD, C. GIRY, F. RAGUENEAU, Strong discontinuity analysis of a class of anisotropic continuum

damage constitutive models–part ii: Concrete material application, Mechanics Research Communications 86 (2017) 27–31.

[67] C. LINDER, F. ARMERO, Finite elements with embedded branching, Finite Elements in Analysis and Design 45 (4) (2009) 280–293.

[68] F. ARMERO, C. LINDER, Numerical simulation of dynamic fracture using finite elements with embedded discontinuities, International Journal of Fracture 160 (2) (2009) 119.

[69] A. RAINA, C. LINDER, A strong discontinuity based adaptive refinement approach for the modeling of crack branching, PAMM 11 (1) (2011) 171–172.

[70] A. FERRER, J. C. CANTE, J. HERNÁNDEZ, J. OLIVER, Two-scale topology optimization in computational material design: An integrated approach, International journal for numerical methods in engineering 114 (3) (2018) 232–254.

[71] A. DELAPLACE, R. DESMORAT, Discrete 3d model as complimentary numerical testing for anisotropic damage, International Journal of Fracture 148 (2) (2007) 115.

Declaration of interests

☒ The authors declare that they have no known competing financial interests or personal relationships that could have appeared to influence the work reported in this paper.

☐The authors declare the following financial interests/personal relationships which may be considered as potential competing interests:

On behalf of all the Authors
Dr Benjamin Richard, HDR Engrg.

Highlights

- A mode to describe intersecting cracks is proposed
- It is based on a transmission between microplane and E-FEM approaches
- Numerical implementation is detailed thoroughly
- Representative case studies are exposed and discussed